



Article

Switching Ion Binding Selectivity of Thiacalix[4]arene Monocrowns at Liquid–Liquid and 2D-Confined Interfaces

Anton Muravev ^{1,*} , Ayrat Yakupov ², Tatiana Gerasimova ¹, Ramil Nugmanov ², Ekaterina Trushina ³, Olga Babaeva ¹, Guliya Nizameeva ⁴, Viktor Syakaev ¹, Sergey Katsyuba ¹, Sofiya Selektor ⁵ , Svetlana Solovieva ² and Igor Antipin ²

- ¹ FRC Kazan Scientific Center, Arbuzov Institute of Organic and Physical Chemistry, Russian Academy of Sciences, Arbuzov Str. 8, 420088 Kazan, Russia; gryaznovat@iopc.ru (T.G.); olbazanova@iopc.ru (O.B.); vsyakaev@iopc.ru (V.S.); katsyuba@iopc.ru (S.K.)
- ² Butlerov Institute of Chemistry, Kazan Federal University, Kremlevskaya Str. 18, 420008 Kazan, Russia; yakupov.airat21@mail.ru (A.Y.); RalNugmanov@kpfu.ru (R.N.); svsol@iopc.ru (S.S.); iantipin54@yandex.ru (I.A.)
- ³ School of Chemistry, University of Glasgow, University Avenue, Glasgow G12 8QQ, UK; kate1809@mail.ru
- ⁴ Department of Physics, Kazan National Research Technological University, Karl Marx Str. 68, 420015 Kazan, Russia; guliya.riv@gmail.com
- ⁵ Frumkin Institute of Physical Chemistry and Electrochemistry, Russian Academy of Sciences, Leninsky pr. 31, 119071 Moscow, Russia; sofs@list.ru
- * Correspondence: antonm@iopc.ru



Citation: Muravev, A.; Yakupov, A.; Gerasimova, T.; Nugmanov, R.; Trushina, E.; Babaeva, O.; Nizameeva, G.; Syakaev, V.; Katsyuba, S.; Selektor, S.; et al. Switching Ion Binding Selectivity of Thiacalix[4]arene Monocrowns at Liquid–Liquid and 2D-Confined Interfaces. *Int. J. Mol. Sci.* **2021**, *22*, 3535. <https://doi.org/10.3390/ijms22073535>

Academic Editor: Taku Shoji

Received: 11 March 2021

Accepted: 25 March 2021

Published: 29 March 2021

Publisher's Note: MDPI stays neutral with regard to jurisdictional claims in published maps and institutional affiliations.



Copyright: © 2021 by the authors. Licensee MDPI, Basel, Switzerland. This article is an open access article distributed under the terms and conditions of the Creative Commons Attribution (CC BY) license (<https://creativecommons.org/licenses/by/4.0/>).

Abstract: Understanding the interaction of ions with organic receptors in confined space is of fundamental importance and could advance nanoelectronics and sensor design. In this work, metal ion complexation of conformationally varied thiacalix[4]monocrowns bearing lower-rim hydroxy (type I), dodecyloxy (type II), or methoxy (type III) fragments was evaluated. At the liquid–liquid interface, alkylated thiacalixcrowns-5(6) selectively extract alkali metal ions according to the induced-fit concept, whereas crown-4 receptors were ineffective due to distortion of the crown-ether cavity, as predicted by quantum-chemical calculations. In type-I ligands, alkali-metal ion extraction by the solvent-accessible crown-ether cavity was prevented, which resulted in competitive Ag⁺ extraction by sulfide bridges. Surprisingly, amphiphilic type-I/II conjugates moderately extracted other metal ions, which was attributed to calixarene aggregation in salt aqueous phase and supported by dynamic light scattering measurements. Cation–monolayer interactions at the air–water interface were monitored by surface pressure/potential measurements and UV/visible reflection–absorption spectroscopy. Topology-varied selectivity was evidenced, towards Sr²⁺ (crown-4), K⁺ (crown-5), and Ag⁺ (crown-6) in type-I receptors and Na⁺ (crown-4), Ca²⁺ (crown-5), and Cs⁺ (crown-6) in type-II receptors. Nuclear magnetic resonance and electronic absorption spectroscopy revealed exocyclic coordination in type-I ligands and cation– π interactions in type-II ligands.

Keywords: thiacalix[4]arene monocrowns; Langmuir monolayers; liquid-phase extraction; ion binding; surface potential; UV/visible reflection–absorption spectroscopy

1. Introduction

Ion binding is of fundamental and practical interest in coordination and supramolecular chemistry, because it involves a multitude of weak interactions and requires an induced fit with the receptor [1,2]. In particular, these features are decisive for efficiency of receptor units pre-organized on a calixarene scaffold [3,4]. Calixarenes have been exploited as ion receptors in liquid-phase extraction, fluorometric sensing, self-assembly on solid surfaces, and coordination network formation [5–8]. Lower-rim modification of calixarenes with oxyethylene units has provided calixarene–crown-ether conjugates (calixcrowns), which display exceptional metal ion binding efficiency and selectivity [9].

Outstanding receptor characteristics of calixcrowns under liquid-phase extraction conditions and structural effects of the macrocycles on binding selectivity were extensively investigated. Selectivity of calix[4]crown-ethers is mainly governed by size complementarity, according to which the crown-4 unit is well suited for Li^+ , while crown-5 and crown-6 units prefer K^+ and Cs^+ , respectively [10,11]. Insofar as monomers are considered, an increase in the number of crown-ether units affects marginally ion extractability of calixcrowns [12]. There is a more complex interplay for steric factors, such as calixarene conformation, upper-rim substitution pattern, and macrocycle cavity size (comparison of calixarenes and thiacalixarenes) [9,13,14]. Such interplay originates from the stabilizing effect of inverted aryl rings in *partial cone* and *1,3-alternate* configurations of calixarene due to ion- π interactions and the destabilizing steric factor from bulky groups at upper/lower rims, the extent of which inversely depends on the calixarene and crown-ether cavity sizes.

More diverse applications of ion-coordinating ability were demonstrated in confined space for calixcrowns functionalized by anchoring groups (Figure 1). One example is *cone* calix[4]crown-5 **I** modified with CH_2SH units on the upper rim, which formed self-assembled monolayers on gold and recognized polyamines [15]. Similarly, *partial cone* analog **II** with dithiolane fragments on the lower rim displayed potentiometric recognition of alkaline-earth vs. alkali metal ions (although the role of crown-ether moiety in such discrimination is not evident) [16]. A different approach was employed in our group to facilitate enzyme adhesion to gold substrate by amphiphilic *1,3-alternate* thiacalix[4]monocrown-5 **III** in Langmuir monolayers [17]. A significant advance in covalent confinement of calixcrowns was achieved through immobilization of thiacycrown **IV**-Au nanoparticles onto polymer membrane to give an ultrasensitive response towards Ag^+ [18]. The groups beyond sulfur functionalities are also used to graft calixcrowns onto the substrates bearing complementary reaction centers. One example is the Cs^+ fluorescence probe based on crown-6 **V** linked to hybrid $(\text{NH}_4)_3\text{PMo}_{12}\text{O}_{40}$ -silica mesoparticles via amide groups [19]. Another example is the calixcrown-ether **VI** monolayer grafted onto silica with a triazole spacer, which demonstrated K^+ -controlled pesticide binding/release monitored by contact angle measurements [20].

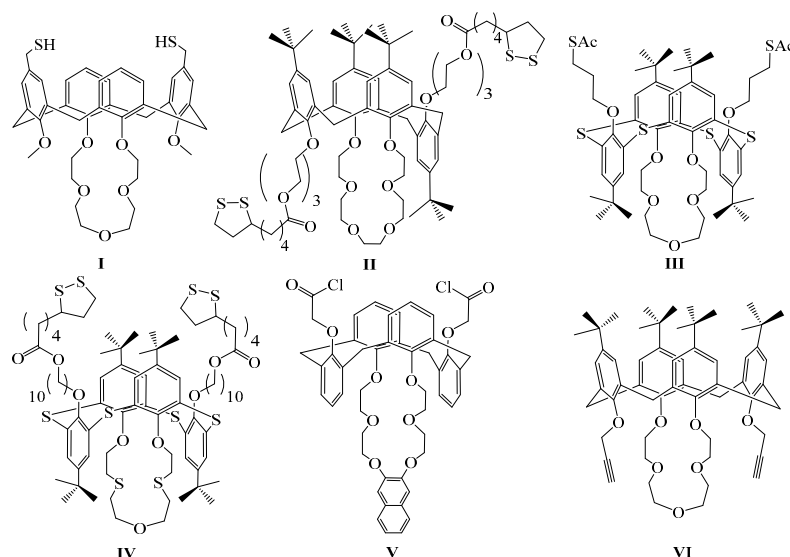


Figure 1. Examples of heterotopic calixcrown-ether receptors with anchoring groups [15–20].

Additional synthetic stages for the attachment of anchoring groups to calixcrowns, as well as their interference in the complexation behavior of crown-ether macrocycle, restrict the choice of metal ions and calixcrowns for the rational design of advanced materials. The Langmuir method, which pre-organizes molecules at the air–water interface and provides tightly packed monolayers under lateral compression, is a convenient tool as it does not require specific anchoring groups and could be effective in evaluating ion binding in thin-

film sensors. There has been a unique study of calixcrown-ethers in Langmuir monolayers, which revealed Cs^+/Na^+ selectivity [21]. Intriguingly, switching of metal ion selectivity in calixarenes with the transition from liquid phase to air–water interface has been recently documented [22]. Thus, comparison of various environments is highly desirable in the study of binding behavior of these host molecules. Here, we report the complexation study of metal ions with topologically varied thiacalix[4]monocrowns at the liquid–liquid interface under extraction conditions and at the air–water interface using the Langmuir monolayer technique.

2. Results and Discussion

2.1. Design, Synthesis, and Characterization of Thiacalix[4]monocrown-Ethers

Figure 2 outlines structural variations in thiacalixcrown-ethers (conformation of macrocycle, number of O atoms in crown-ether, and alkyl chain length). Three structural types were considered:

- (1) Ionizable *cone* thiacalixcrowns, with four to six oxygen atoms in the crown-ether ring (type I);
- (2) Amphiphilic *1,3-alternate* thiacalixcrowns bearing C_{12} -chain at the lower rim (type II);
- (3) Conformationally flexible thiacalixcrowns bearing OMe groups at the lower rim (type III).

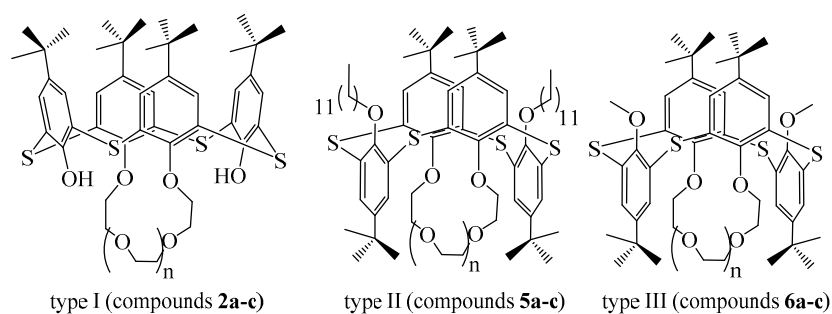
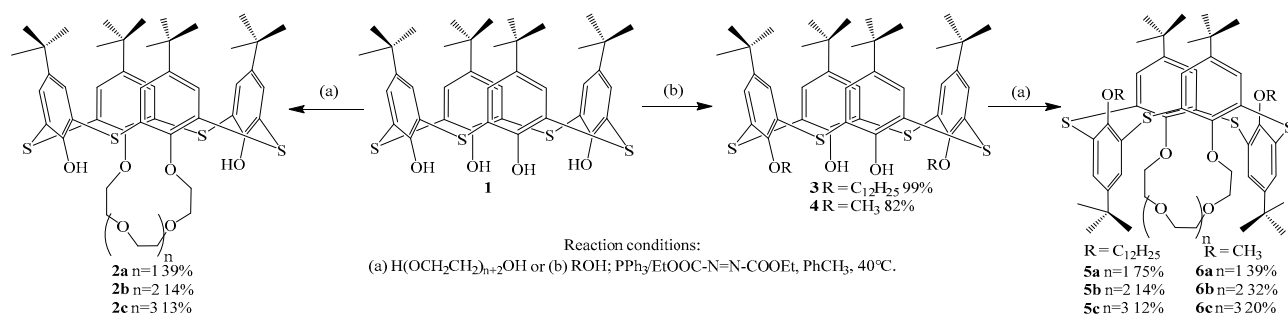


Figure 2. Type I–III thiacalix[4]monocrowns studied in this work ($n = 4–6$).

Crosslink of distal OH groups of thiacalixarene with oligoethylene glycols using triphenylphosphine and diethyl azodicarboxylate system (Mitsunobu reaction) or ditosylates through K_2CO_3 -mediated nucleophilic substitution is a common macrocyclization route into thiacalixcrowns [23,24]. Former approach is preferable for dialkylated thiacalixarene precursors, because ether groups can be cleaved in alkaline medium at high temperature [25]. Type-I thiacalixcrowns **2a–c** were synthesized as previously reported from thiacalixarene **1** and tri-, tetra-, and pentaethylene glycol (Scheme 1) [23]. Given low yields of thiacalixcrowns **2b,c**, alkyl fragments were firstly attached to compound **1** to access type-II/III ligands. Dialkylated products **3** and **4** were synthesized as reported previously [26,27] and further reacted with the glycols (Scheme 1). Type-II/III crown-ethers **5b,c** and **6b,c** were isolated in low yields (12–32%), while yields of crown-4 **5a** and **6a** were 75% and 39%, respectively. These results agree with the reported increase in the yield of crown-4 derivatives as compared to larger crown-ethers, forming open-chain products and calixtubes [28,29].



Scheme 1. Synthesis of thiacalixcrown-ethers.

The physical characteristics of ligands **2a–c** coincide with the literature data [23] and indicate *cone* configuration due to the large chemical shift (CS) difference of aryl and *t*-Bu groups in ^1H nuclear magnetic resonance (NMR) spectra. Intramolecular [1+1]-macrocyclization follows from matrix-assisted laser desorption–ionization (MALDI) mass peaks at m/z 857–946 (Figures S1–S6). CS of OH group in crown-4 **2a** is quite large as compared to that in crowns **2b,c** (8.46 ppm vs. 8.00–8.10 ppm) (Figure S1). Such features of dialkylated thiacalix[4]arenes were previously mentioned [30] and indicate that ligand **2a** exists as *pinched cone* (PC) stereoisomer, while ligands **2b,c** adopt *distorted cone* (DC) conformation (Figure S27). The structures of new ligands **5a–c** were assigned by $^1\text{H}/^{13}\text{C}$ NMR and infrared (IR) spectroscopy and MALDI mass spectrometry (Figures S7–S18). An example ^1H NMR spectrum of ligand **5c** (Figure 3) shows a small CS difference of aryl and *t*-Bu protons (0.03–0.06 ppm) and upfield signals of ArOCH_2 protons with respect to compound **2c** due to magnetic anisotropy of proximal inverted aromatic rings (4.01 vs. 4.74 ppm), which indicates *1,3-alternate* conformation. The crown-ether bridge peak order is another empirical criterion for elucidation of stereoisomeric form of thiacalixcrowns [24]. Namely, if the protons of oxyethylene unit next to aromatic ring are downfield with respect to other crown-ether protons, calixarene adopts the *cone* conformation, whereas these protons are most down- and upfield peaks in *1,3-alternate* conformation. In contrast to *cone* **2c** with peak order of 13–14–15–16–17 (Scheme S1), this order is 3–7–5–6–4 in *1,3-alternate* **5c** (Figure 3).

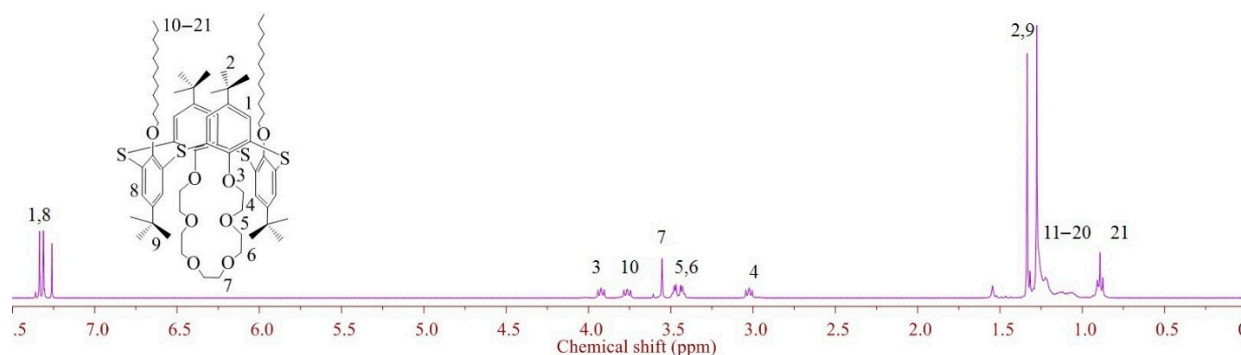


Figure 3. ^1H NMR spectrum of compound **5c** in CDCl_3 at 293 K.

Monocrowns **6a–c** were originally identified as *1,3-alternate* stereoisomers due to high-symmetry ^1H NMR spectra [13,24]. However, such assignment is in apparent contradiction with conformationally flexible thiacalix[4]arenes, bearing larger units at the lower rim [31,32]. NMR spectra reveal high-field shift of OMe group at 3.30–3.50 ppm, a large CS difference between the protons of benzene ring (0.14–0.19 ppm in crowns **6a,b** vs. 0.03 in crowns **5a,b**) and *t*-Bu groups (0.18 ppm in crown **6c** vs. 0.05 in crown **5c**), and violated crown-ether peak order in compounds **6b,c** (Figures S19–S21). These factors highlight that anisole rings decline from macrocycle rim and deshield aryl protons, whereas OMe groups approach proximal benzene rings of the macrocycle and shield them. Such behavior can be

rationalized by a fast 1,3-alternate-partial cone equilibrium. This suggestion is confirmed by a 1,3-alternate-to-partial cone transformation upon crystallization of compound 6c [24].

2.2. Complexation of Metal Ions at Liquid–Liquid Interface

Previously reported results of extraction of thiocalixcrowns 2b and 6b,c [13,33] cannot be compared due to different organic phase and component ratio. Thus, liquid-phase extraction of alkali metal and Ag picrates by type I–III ligands was carried out (Figure 4a). All the ligands extracted Ag^+ , with the degree of extraction from 9% in crown-4 6a to 61% in crown-6 2c. The main reason for Ag^+ extractability is that S atoms are not much solvated in the aqueous phase. However, alkali metal ion extractability is governed by thiocalixcrown topology. Solvent-accessible crown-ether cavity in type-I cone thiocalixcrowns 2a–c is influenced by the solvation of adjacent ionizable OH-groups along with H-bonding of aryl O atoms with OH groups. These factors lead to the higher energy of complexation involving desolvation of receptor fragment. Indeed, group IA metal ions were hardly extracted by compounds 2a,b. Crown-6 macrocycle of compound 2c is hindered by OH groups to a lower extent than smaller crown-ethers and displayed a group selectivity towards K^+ , Rb^+ , and Cs^+ , the extraction of Rb^+ (33%) being highest. Such selectivity can be rationalized by lower free energy of transfer of Cs (25.73 $\text{kJ} \times \text{mol}^{-1}$), Rb (27.57 $\text{kJ} \times \text{mol}^{-1}$), and K (36.52 $\text{kJ} \times \text{mol}^{-1}$) picrates to CH_2Cl_2 compared to NaPic (61.84 $\text{kJ} \times \text{mol}^{-1}$) [34] and similar sizes of crown-ether and Rb^+ ($d_{\text{Rb}^+} = 3.1 \text{ \AA}$ [35]; $d_{\text{crown}} = 3.2 \text{ \AA}$ [36]).

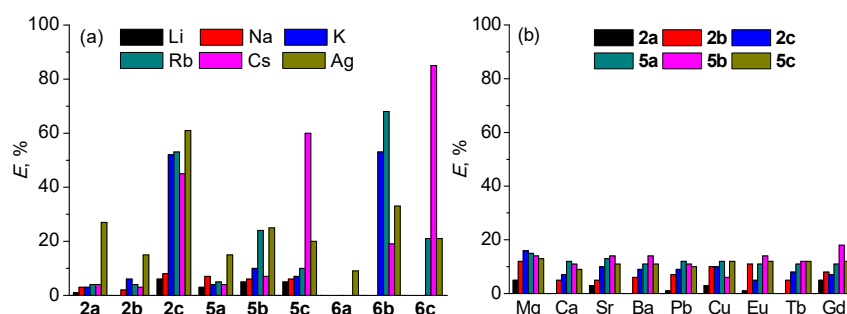


Figure 4. Degree of extraction (E , %) of (a) alkali metal picrates (pH = 12) and AgPic (pH = 7) by compounds 2, 5, and 6 and (b) other metal picrates (pH = 5.8, tris buffer) by compounds 2 and 5. $c_M = 2 \times 10^{-4} \text{ M}$, $c_L = 4 \times 10^{-4} \text{ M}$. The error is less than 2%.

A decisive role of solvation of type-I crown-ethers and metal ions in extraction was confirmed by the gas-phase analysis of crown-ethers 2a–c with the mixture of metal nitrates (Figure 5). Under competitive conditions, the size complementarity of crown-ether and ion was revealed. Most intense mass peaks corresponded to the complexes of 2a– Li^+ , 2b– Na^+ , and 2c– K^+ . All metal salts showed mass peaks corresponding to crown-ether complexes when added separately (Table S1), which excludes the factors beyond complexation, e.g., instability of molecular ions with other metals. Thus, Ag^+ or alkali cation selectivity of compounds 2a–c is governed by charge interactions with crown-ether and OH moieties in the gas phase and orbital interactions with sulfide bridges at the liquid–liquid interface.

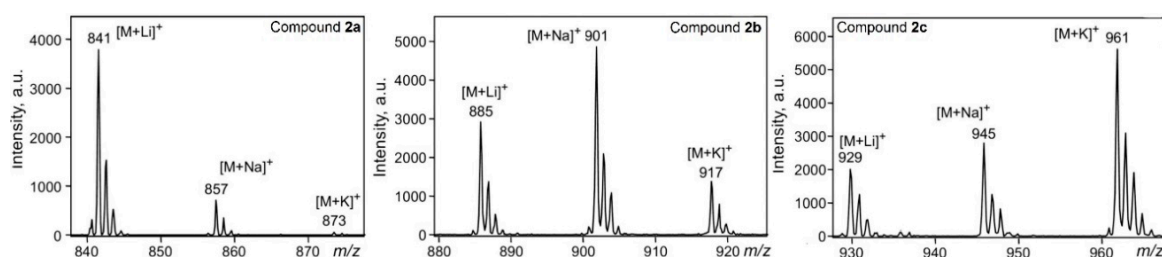


Figure 5. Matrix-assisted laser desorption–ionization (MALDI) mass spectra of the ligands 2a–c mixed with metal nitrate salts.

In type-II/III ligands, crown-ether cavity is hindered from solvent molecules by *t*-Bu groups and benzene rings and impact of solvation on alkali metal extraction selectivity could be lower and resemble gas-phase ion selectivity. Extraction experiments confirm this suggestion and ionic radius–crown-ether size correlation was observed, with the highest degree of extraction of K^+/Rb^+ by crown-5 receptors **5b** and **6b** and Cs^+ by crown-6 receptors **5c** and **6c**. The reported alkali metal ion extraction selectivity of crown-ethers **6b,c** at higher concentrations (10^{-3} M) [13] agrees with extraction data of this work and gas-phase complexation of 1,3-alternate thiacalixcrowns **5a–c**, which were selective towards Na^+ , K^+ , and Cs^+ , respectively (Figure S22). A different size complementarity of metal ions with compounds **5a–c** and **2a–c** in the gas phase is presumably caused by different accessibility of crown-ether units and ion coordination by phenyl rings in former case and OH groups in latter case.

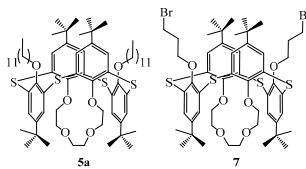
Unlike thiacalixcrowns-5(6), crown-4 ligands are poor extractants, which indicates the role of the factors other than solvent accessibility of crown-ether macrocycle. Quantum-chemical modeling of Li^+ complexes of 12-crown-4 and compounds **2a/6a** (Table S2) revealed their different shapes. In contrast to Li^+ complex of 12-crown-4, where the d_{Li-O} is ca. 2.0 Å and d_{O-O} are ca. 2.7 Å, the crown-ether in ligands **2a/6a** is distorted, with distances of 4.1–4.6 Å between distal O atoms. Such expansion of crown-ether increases Li–O bond lengths and results in less effective binding. Although OH group in ligand **2a** can coordinate cations, the complexation constant should be low due to entropic penalty.

Surprisingly, ligands **2** and **5** could extract all cations, which is in sharp contrast to the behavior of compounds **6b,c** and other 1,3-alternate (thia)calix[4]crowns [13]. The scope of ions was extended to group-II metal ions, Pb^{2+} , Cu^{2+} , and lanthanide ions and 5 to 20% of these ions were extracted into CH_2Cl_2 (Figure 4b). With regards to ion extraction by type-I ligands **2a–c**, high pH at which phenolate anions could be involved in charge interactions with metal ions needs to be considered. Moreover, amphiphilic ligands **2a–c** and **5a–c** could display surface activity, which is discussed in Section 2.3.

2.3. Aggregation of Crown-Ether Ligands with and without Metal Ions

Exact mechanism of metal ion extraction is yet unclear, but assistance of complexation-induced micelle formation in the aqueous phase [37] and organic phase [38,39] to the metal ion transfer through the water–oil interface was claimed and recently reviewed [40]. A number of methods was employed to ensure the absence of calixcrown aggregates in organic solvent before establishing the role of aggregation in cation extraction. The dynamic light scattering (DLS) technique showed no spherical particles of crown-ethers **2**, **5**, and **6** in $CHCl_3$ at $c = 4 \times 10^{-4}$ M. Formation of true solutions of type-II ligands **5** was supported by Fourier transform pulsed-gradient spin-echo (FT-PGSE) NMR experiments. Self-diffusion constants of amphiphilic calixarene **5a** and reference compound **7** [29] are similar in $CDCl_3$ at higher concentrations and their aggregation numbers are close to 1 (Table 1).

Table 1. Diffusion coefficients (D_s), hydrodynamic radii (R_h), and aggregation numbers (N_{aggr}) of calixarenes **5a** and **7** in $CDCl_3$ ($T = 303$ K).

	$c, 10^{-3}M$	$D_s, 10^{-10} m^2/s$	$R_h, \text{Å}$	N_{aggr} (from c_{min})
5a	5	6.10	7.2	1.0
	30	5.67	7.8	1.2
	5	7.61	5.8	1.0
	30	6.59	6.7	1.5

Having excluded the aggregation of calixcrowns in individual solvent before extraction, particle size distribution (PSD) in CH_2Cl_2 and aqueous phases after their mixing was analyzed. Table 2 shows number-averaged PSD of crown-6 **2c**, **5c**, and **6c** after mixing in CH_2Cl_2 –water system with and without Cs salts (PSD plots and correlation functions are given in Figures S23–S25). There is a different pH in blank aqueous phase ($pH \approx 7$) and the aqueous phase with CsPic ($pH \approx 12$); moreover, there is a possible effect of Pic^- on the

aggregation of calixcrowns. Therefore, CsNO₃ was also tested due to its neutral pH, which allows for a direct evaluation of the role of Cs⁺ on the PSD.

Table 2. Number-averaged PSD of thiacalix[4]crowns **2c**, **5c**, and **6c** after stirring in CH₂Cl₂–water.

Compound	Analyzed Phase	Metal Salt	Size, nm	Polydispersity Index
2c	CH ₂ Cl ₂ and Water	–/CsPic	–	–
	CH ₂ Cl ₂	CsNO ₃	313.1 ± 14.5	0.95 ± 0.05
	Water	CsNO ₃	298.7 ± 36.7	0.39 ± 0.08
5c	CH ₂ Cl ₂	–	285.4 ± 32.1	1.00
		CsPic	426.4 ± 26.1	0.47 ± 0.09
		CsNO ₃	165.9 ± 34.1	0.45 ± 0.18
	Water	–	–	–
		CsPic	80.9 ± 5.6	0.46 ± 0.04
		CsNO ₃	262.7 ± 21.5	0.37 ± 0.06
6c	CH ₂ Cl ₂	–	–	–
		CsPic	76.3 ± 15.2	0.59 ± 0.13
		CsNO ₃	259.3 ± 58.3	0.36 ± 0.23
	Water	–	331.3 ± 38.2	0.30 ± 0.05
		CsPic/CsNO ₃	–	–

Blank experiments with Cs salts verified the absence of any aggregates after mixing CH₂Cl₂ with aqueous salt solutions. When thiacalixcrowns were dissolved in CH₂Cl₂, true solutions were no longer detected. After mixing with water, type-I ligands with OH-groups formed microparticles in CH₂Cl₂ resulting in the turbid organic phase. Lipophilic dodecyl derivative **5c** formed polydisperse nanoassociates in CH₂Cl₂ with the $R_h = 142$ nm and no aggregates in the aqueous phase. More hydrophilic methoxy derivative **6c** assembled into 300-nm aggregates in the aqueous phase, whereas only microparticles were detected in CH₂Cl₂. It can be hypothesized that mixed solvent alters hydrophilic–lipophilic balance of calixcrowns due to inclusion of solvent into macrocycle cavity and facilitates aggregation in the form of microemulsion. The density functional theory (DFT) study of solvation of crown-6 receptors confirms that macrocycle **5c** is most lipophilic, with the $\Delta G = 96.23$ kJ \times mol^{−1} between CHCl₃ and water, whereas the energy gap corresponds to 46.02 and 20.92 kJ \times mol^{−1} in ligands **2c** and **6c**. Thus, the results of DFT calculations rationalize the absence of aggregates of **2c/5c** in the aqueous phase due to low probability of crossing the water–oil boundary.

Two trends became visible on addition of Cs salts to the aqueous phase. Firstly, nanoassociates were detected in the organic phase after extraction, which suggests complexation-induced aggregation of calixcrowns after metal-ion transport through the oil/water interface. Secondly, and more interestingly, the aggregates of type-I/II amphiphiles **2c** and **5c** were also detected in the aqueous phase, whereas type-III compound **6c** did not form nanoassociates and no particles were detected in the aqueous phase after extraction of Cs salt. The particle size in the aqueous phase after CsNO₃ extraction by both types of amphiphilic ligands was ca. 300 nm with a polydispersity index of ca. 0.4. The mean aggregate size in the aqueous phase decreased to 81 nm when CsPic was extracted by dodecyl derivative **5c**, which is presumably caused by higher lipophilicity of Pic[−] as compared to NO₃[−]. In contrast, no aggregates of ionizable thiacalixcrown-6 **2c** with CsPic were detected in both phases at high pH due to phenolate ion formation, which disfavors the association of Cs⁺ complexes.

Analysis of PSD showed the connectivity of aggregation phenomena with metal ion extraction by amphiphilic calixcrowns and agrees with literature data on Am³⁺ and Cs⁺ selective calix[8]arenes [41] and Ag⁺-selective thiacalixtubes [42]. In spite of insufficient data set to establish the mechanism of picrate extraction, the results of DLS in the aqueous phase suggest nonspecific inclusion of metal picrates to calixcrown aggregates, which leads to their nonzero extractability. In contrast to type-I/II receptors, disappearance of nanoassociates of flexible methoxy derivative **6c** on addition of salt to the aqueous phase

agrees with the proposed mechanism of Cs^+ extraction by methoxy derivative of calixcrown counterpart “right at the interface” [43] and is presumably caused by the salting-out effect, which increases the critical aggregation concentration of compound **6c** in the aqueous phase.

The statements derived from the DLS study of type I–III crown-6 receptors after Cs^+ extraction were also valid for other metal salts, such as NaPic and RbPic. In spite of low degree of Na^+ and Rb^+ extraction, nanoaggregates were detected in type-I/II conjugates in contrast to type-III methoxy derivative (Figure S26). Thus, evidence that nonzero metal ion extractability by type-I/II crown-ether receptors is related to surface activity in the aqueous phase was provided.

2.4. Langmuir Monolayer Formation

Formation of true solutions of the thiacalixcrowns in CHCl_3 indicated its feasibility as a spreading solvent to form Langmuir monolayers at the air–water interface. The importance of the absence of aggregates in spreading solution for true monolayer production was recently demonstrated for nitrothiacalix[4]arenes [44]. Structural optimization of the thiacalixcrowns using molecular mechanics (Figure S27) shows that type-I crown-ethers **2a–c** occupy the area of ca. 200 \AA^2 per molecule at parallel orientation of C_{2v} axes of molecules relative to water subphase, whereas *1,3-alternate* ligands occupy ca. 250 \AA^2 (dodecyloxy derivatives **5a–c**) and $125\text{--}163 \text{ \AA}^2$ (methoxy derivatives **6a–c**) at the same orientation (Table 3, parameter A_{\parallel}). Therefore, aliquots of $1 \times 10^{-4} \text{ M}$ solutions of crown-ether receptors in CHCl_3 were spread over water subphase to give the starting molecular area larger than their parallel orientation and surface pressure/surface potential (SPOT)–molecular area isotherms were recorded upon monolayer compression (Figure 6).

Table 3. Monolayer characteristics of calixarenes **2**, **5**, and **6** (take-off area A_0 , compression modulus C_s^{-1} , calculated molecular area at vertical (A_{\perp}) and horizontal orientation (A_{\parallel}), surface potential (ΔV), surface dipole moment (μ_{\perp}), and maximum absorbance (λ_{max})).

Ligand	$A_0, \text{ \AA}^2$	$C_s^{-1}, \text{ mN/m}$	$A_{\perp}, \text{ \AA}^2$	$A_{\parallel}, \text{ \AA}^2$	$\Delta V, \text{ mV}^3$	$\mu_{\perp}, \text{ D}$	$\lambda_{\text{max}}, \text{ nm}$
2a	195 ± 6	40	117^1	162	508	1.35	302
2b	182 ± 5	50	104^2	171	517	1.37	303
2c	176 ± 5	37	103^2	193	740	1.96	304
5a	201 ± 6	29	129	240	263	0.70	271
5b	185 ± 6	27	132	252	295	0.78	269
5c	177 ± 5	45	127	250	375	0.99	271
6a	392 ± 12	25	109	122	225	1.19	270
6b	467 ± 14	38	108	149	281	1.49	271
6c	506 ± 15	42	103	163	301	1.60	270

¹ Calculated for PC conformer; ² calculated for DC conformer; ³ at the molecular area of 100 \AA^2 (**2**, **5**) and 200 \AA^2 (**6**).

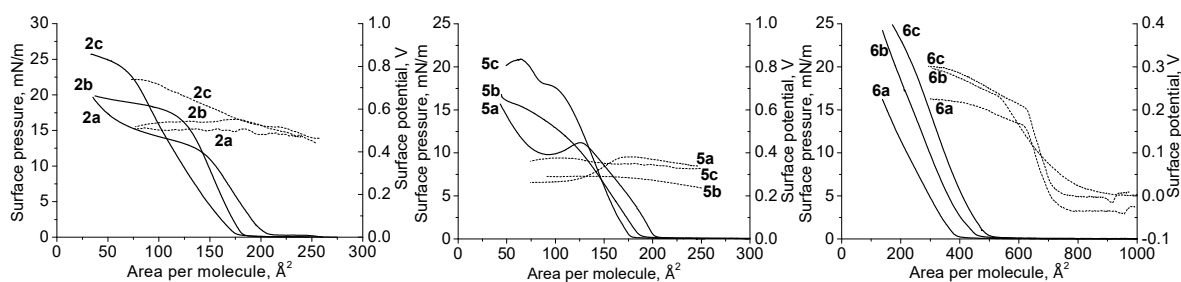


Figure 6. Surface pressure/surface potential (SPOT)–molecular area isotherms of compounds **2a–c**, **5a–c**, and **6a–c** at the air–water interface ($c = 1 \times 10^{-4} \text{ M}$ (**2a–c**, **5a–c**) and $1 \times 10^{-5} \text{ M}$ (**6a–c**) in CHCl_3).

The ligands formed rigid monolayers with an upward trend between the size of the crown-ether unit and the bend pressure of monolayer isotherms due to the increase in

hydrophilicity and size of the crown-ether macrocycle (Figure 6). Compression moduli (C_s^{-1}) of the ligands are 25–72 mN/m, which corresponds to the liquid-expanded state of the monolayers [45]. UV/visible reflection–absorption spectra (UVRAS) of ligands **5a–c** and **6a–c** in monolayers are similar to their electronic absorption in CHCl_3 ($\lambda_{\text{max}} = 270\text{--}273$ nm) (Figure S29a,b), whereas the absorbance maximum in spectra of compounds **2a–c** appears at 302–304 nm. To ensure that this absorbance maximum corresponds to the second band in solution spectra rather than a red-shifted band at 284 nm due to solvatochromism, the MeOH cosolvent was gradually added to 1×10^{-4} M solution of compound **2c** in CH_2Cl_2 . As expected, no shift of the absorbance peaks at 281 and 303 nm was observed (Figure S29c).

Type-I/II ligands **2a–c** and **5a–c** are amphiphilic and crown-ether cavity should be immersed into water subphase upon spreading, with the perpendicular orientation of C_{2v} axes relative to the water surface, which is confirmed by the surface dipole moment of 0.7–2.0 D from SPOT measurements. The take-off area of compounds **5a–c** (177–201 \AA^2) is less than the calculated area of parallel-oriented molecules, whereas the take-off area of compounds **2b,c** (176–182 \AA^2) is similar to parallel orientation (Table 3). Crown-4 **2a** is characterized by larger take-off area (195 \AA^2) due to *PC* conformation of thiacalixarene, whose calculated area (A_{\perp}) is largest among type-I receptors (117 \AA^2 vs. 103–104 \AA^2). Unlike compounds **2** and **5**, the orientation of less lipophilic type-III ligands **6a–c** in monolayer is unclear a priori. These compounds did not form reproducible Langmuir monolayers at the spreading area of 300 \AA^2 per molecule. Therefore, their spreading area was increased up to 1000 \AA^2 to give true monolayers with the takeoff areas of 400–500 \AA^2 per molecule. These differences in mean molecular areas appear to be related to significant conformational changes in the molecules of compounds **6a–c** (previously mentioned in Section 2.1) upon transition from the organic phase to the air–water interface. Similar values were reported for non-amphiphilic terpyridine-thiacalix[4]arenes [46].

Upon monolayer compression, the SPOT values of ligands **2a–c** and **5b,c** increase slightly from ca. 450 mV and 100–200 mV, respectively, before collapsed state of monolayer, which shows dipole ordering at spreading areas and no further reorientation. The SPOT values of ligand **5a** gave a downward trend at $\pi > 6$ mN/m, indicative of onset of multilayer formation. In contrast, near-zero SPOT values of type-III compounds **6a–c** at the spreading areas suggest no aggregates/islands in monolayers. Moreover, critical molecular areas corresponding to a drastic rise of SPOT and structuring of monolayer in the form of islands (700–800 \AA^2) are much higher than take-off areas in π -*A* isotherms (400–500 \AA^2).

Compression–expansion cycles were carried out to assess molecular interactions in a monolayer (Figure 7). No hysteresis loop was recorded in type-I calixcrown **2c**, which indicates a weak interaction between calixarene molecules and reversibility of the monolayer. A slight loss in the take-off area after the first cycle may result from residual patches in film after expansion. Normalized area relaxation curves (Figure S28) demonstrated high stability of compound **2c** monolayer near collapse pressures and no loss of molecular area over time. This fact indicates weak interactions and is in good agreement with the abovementioned behavior of compound **2c**, whose molecules do not form 3D aggregates at high surface pressures. In contrast, monolayer of ligand **5c** is evidently stabilized by hydrophobic interactions between dodecyl chains and a hysteresis loop was observed. These interactions are strong enough to change the monolayer irreversibly, because there is a drop of collapse pressure after the second compression cycle (15 ± 1 mN/m). A decisive role of C_{12} -chains of crown **5c** rather than stacking of aryl rings in stabilization of associates formed upon monolayer compression was confirmed by nearly identical compression–expansion isotherms of methoxy counterpart **6c**.

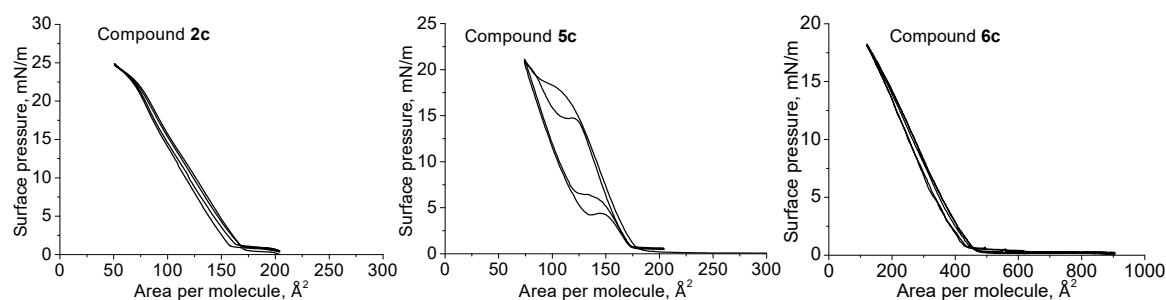


Figure 7. Monolayer compression–expansion cycles of compounds **2c**, **5c**, and **6c** at the air–water interface ($c = 1 \times 10^{-4} M$ (compounds **2c** and **5c**) and $1 \times 10^{-5} M$ (compound **6c**) in CHCl_3).

The monolayers of ligands **2**, **5**, and **6** were deposited onto quartz wafer using the Langmuir–Blodgett technique. The transfer ratio (TR) was close to unity (Table 4) and indicated complete transition of the monolayers from air–water interface to substrate. Morphological characterization of the monolayers by atomic force microscopy (AFM) revealed formation of quasi-continuous films, with the 100–200 nm associates that are 3 to 9 nm in height (as indicated by pseudocolor scale) (Figures S31–S35). Surface roughness R_a , which could be regarded as effective thickness of such films, corresponds to 0.25 to 2.50 nm and exceeds that of bare quartz (0.20 nm, Figure S30), showing that there is one-molecule-thick film.

Table 4. Morphological characteristics of bare quartz and quartz coated with Langmuir–Blodgett films of ligands **2a–c**, **5a–b**, and **6a**. The concentration of the spreading solution is given in parentheses.

Compound	Number of Monolayers	R_a , nm	h , nm	TR	π_{transfer} , mN/m
quartz	n/a	0.20	n/a	n/a	n/a
2a ($1 \times 10^{-5} M$)	1	0.30	n/a	0.76	10
2b ($1 \times 10^{-5} M$)	1	0.25	n/a	0.93	12
5a ($1 \times 10^{-5} M$)	1	2.3	n/a	0.84	6
5b ($1 \times 10^{-5} M$)	1	2.5	n/a	1.15	12
6a ($1 \times 10^{-5} M$)	1	1.0	n/a	0.98	10

2.5. Metal Ion–Monolayer Interactions at the Air–Water Interface

The electrostatic repulsion of metal ions in the monolayer and its further destabilization make it convenient to analyze the change of π – $A/\Delta V$ – A isotherms in conformationally fixed calixarenes over salt water subphase as a criterion of ion–monolayer interactions [47]. Optical response could also be useful to evaluate cation– π interactions in type-II thiacalixcrowns and monitor changes of calixarene conformation and aggregation. Thus, surface pressure and SPOT isotherms along with UVRAS were recorded to analyze ion uptake at the air–water interface. Complexation of calixarenes **2a–c** and **5a–c** was studied by spreading the ligand from the organic solvent over the water subphase containing metal nitrates and subsequent monolayer compression; take-off areas of the ligands are given in Table 5.

Langmuir monolayers of type-I crown-4 **2a** marginally change the take-off area of 195 \AA^2 in the presence of most metal ions in water subphase, which agrees with the predicted distortion of crown-ether cavity (Table S2). However, the monolayer expanded significantly in the presence of $\text{Ba}(\text{NO}_3)_2$ and $\text{Sr}(\text{NO}_3)_2$ in the water subphase, which gave the values of 226 and $241 \text{ \AA}^2/\text{molecule}$ (Figure 8). In addition, SPOT values of the monolayer of compound **2a** increased in the presence of $\text{Sr}^{2+}/\text{Ba}^{2+}$, $580/710 \text{ mV}$ vs. 508 mV over deionized water (Figure 7) due to the decrease in the negative contribution of the double-layer potential of ionized monolayers. Given the small size of the crown-4 cavity, the binding of these ions could be rationalized by exocyclic coordination with OH groups and a crown-ether fragment. The distances between oxygen atoms of the crown-ether ring

and OH groups are ca. 3.0 Å in compound **2a** (Table S2), which fit well Ba²⁺ and Sr²⁺ ions ($d_{\text{ion}} = 2.36\text{--}2.70$ Å [35]).

Table 5. Take-off areas A_0 of ligands **2a–c** and **5a–c** on the water subphase containing 1×10^{-2} M metal nitrates. Deviation of the area was less than 3%.

Ion (r , Å) ¹	A_0 , Å ²					
	2a	2b	2c	5a	5b	5c
–	195 ± 6	182 ± 5	176 ± 5	201 ± 6	185 ± 6	177 ± 5
Li ⁺ (0.76)	213 ± 6	200 ± 6	181 ± 5	201 ± 6	188 ± 6	178 ± 5
Na ⁺ (1.02)	187 ± 6	173 ± 5	172 ± 5	234 ± 7	211 ± 6	179 ± 5
K ⁺ (1.38)	205 ± 6	264 ± 8	211 ± 6	215 ± 6	178 ± 6	181 ± 5
Rb ⁺ (1.53)	189 ± 6	238 ± 7	207 ± 6	228 ± 7	208 ± 6	197 ± 6
Cs ⁺ (1.67)	195 ± 6	208 ± 6	211 ± 6	211 ± 6	192 ± 6	212 ± 6
Mg ²⁺ (0.72)	192 ± 6	186 ± 5	172 ± 5	220 ± 6	192 ± 6	183 ± 6
Ca ²⁺ (1.00)	201 ± 6	189 ± 5	177 ± 5	235 ± 7	228 ± 8	199 ± 6
Sr ²⁺ (1.18)	241 ± 7	200 ± 6	177 ± 5	213 ± 6	197 ± 6	181 ± 5
Ba ²⁺ (1.35)	226 ± 7	180 ± 5	178 ± 5	211 ± 6	210 ± 6	184 ± 6
Pb ²⁺ (1.19)	190 ± 6	214 ± 6	195 ± 6	221 ± 6	204 ± 6	179 ± 5
Ag ⁺ (1.15)	221 ± 7	181 ± 5	223 ± 7	190 ± 6	191 ± 6	180 ± 5
Eu ³⁺ (0.95)	203 ± 6	182 ± 5	179 ± 5	212 ± 6	182 ± 6	176 ± 5
Tb ³⁺ (0.94)	203 ± 6	206 ± 6	180 ± 5	205 ± 6	193 ± 6	178 ± 5
Gd ³⁺ (0.92)	204 ± 6	214 ± 6	180 ± 5	211 ± 6	179 ± 6	178 ± 5

¹ Effective ionic radius [35].

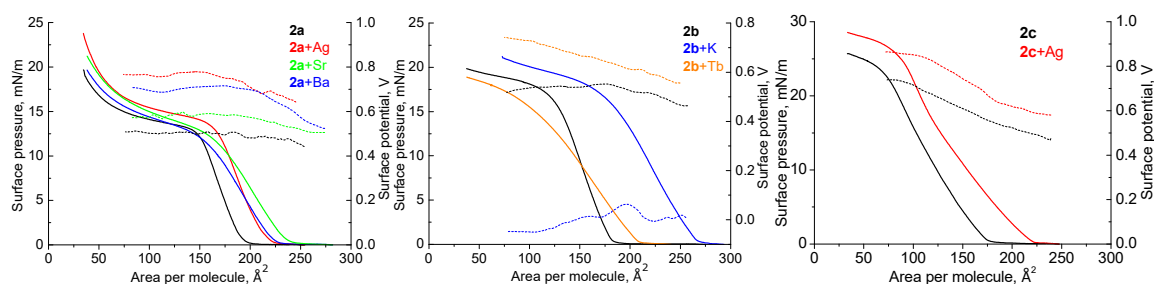


Figure 8. Surface pressure/SPOT–molecular area isotherms of monolayers of thiacalixcrowns **2a–c** on water or 1×10^{-2} M salt water subphase. Concentration in CHCl₃ is 1×10^{-4} M.

The monolayer of crown-5 **2b** expanded in the following order: K⁺ > Rb⁺ > Cs⁺ (Figure 8), while minor changes were observed with alkaline-earth metal ions (Table 5). The ΔV_{max} value of compound **2b** with K⁺, Rb⁺, and Cs⁺ decreased from 517 to –50, –8, and 155 mV, which can be related to the conformational change of the crown-ether ring. The recovery of alkali metal uptake by this ligand could be associated with a near-neutral pH, at which the crown-ether macrocycle is less solvated than at high pH values used for picrate extraction (pH = 12) due to OH groups, in addition to increased steric hindrance from solvent molecules due to lateral compression. More compressible monolayers were recorded over the Pb²⁺/Tb³⁺ salt water subphase and SPOT increased to ca. 740 mV. A decrease in the C_s^{-1} values of the latter monolayers can be caused by ion binding by OH groups through deprotonation. The fact that all metal ions, which expanded the monolayer of compound **2b**, are larger than Na⁺ (except for Li⁺), which was effectively encapsulated by the crown-5 cavity of thiacalixarene in the gas phase (Figure 5), again suggests exocyclic coordination of metal ions with crown-ether and OH moieties.

The largest monolayer expansion of crown-6 **2c** was recorded over water subphase containing AgNO₃ (Figure 8), the collapse pressure of monolayer increased from 22 to 24 mN/m, and ΔV_{max} value also increased from 740 to 860 mV, whereas K⁺, Rb⁺, and Cs⁺ expanded the monolayer of compound **2c** to a lower extent. Thus, there is an apparent Ag⁺ binding of compound **2c** at the air–water interface. UVRAS spectra of the monolayers over

different subphases were nearly identical, which indicates retention of the conformation of calixarene macrocycle (Figure S36a).

Unlike type-I ligands, cation- π interactions could govern metal ion uptake of *1,3-alternate* thiacalixcrowns due to proximity of aryl rings to crown-ether macrocycle, which is particularly important in the case of alkaline-earth metal ions [48]. Na^+ and Ca^{2+} salts shifted the pressure–area isotherm to larger areas and increased surface potential of type-II thiacalixcrown **5a** (Figure 9). Similarly, the largest monolayer expansion of crown-5 **5b** was recorded in the presence of Ca^{2+} , and SPOT increased to 376 mV. A red shift of the absorption band from 273 to 290 nm in UVRAS spectra at high surface pressures indicates either cation- π interactions of Ca^{2+} with benzene rings of thiacalixcrown **5b** (previously indicated in metal complexes of *1,3-alternate* calixcrowns [9]) or aggregation of molecules (there is a shoulder band in UV/visible spectra of the ligands at 290 nm), whereas UVRAS spectra of compounds **5a** and **5c** did not change over salt water subphase (Figure S36b–d). Ca^{2+} binding by crown-ethers in type-II ligands **5a,b** reveals the contribution of the pre-organization of calixarene in the *1,3-alternate* configuration to favor cation- π interactions and Ca^{2+} –crown-ether size complementarity. When there is CsNO_3 in the water subphase, the monolayer of crown-6 **5c** is expanded to the take-off area of 168 \AA^2 , whereas ΔV_{max} increases to 509 mV. The kink at $\pi = 10 \text{ mN/m}$ is accompanied by the onset of SPOT decrease, which suggests the onset of multilayer formation.

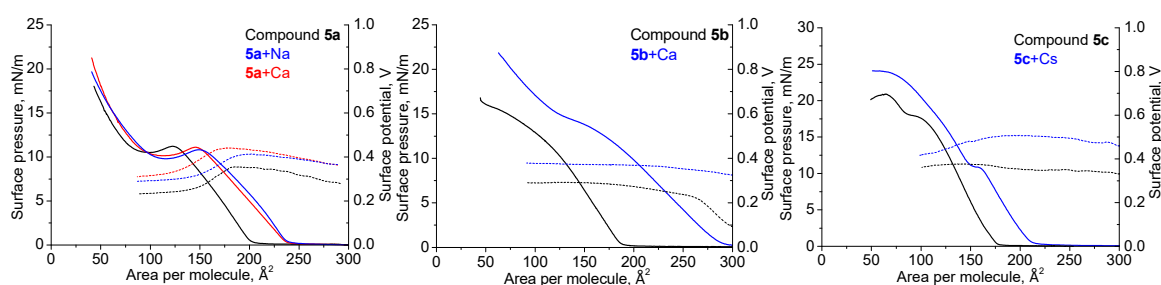


Figure 9. Surface pressure/SPOT–molecular area isotherms of thiacalixcrowns **5a–c** on water or 0.01 M aqueous salt solution subphase. The concentration in CHCl_3 is $1 \times 10^{-4} \text{ M}$.

Type-III ligands **6a–c** displayed opposite trends in surface pressure–area isotherms (monolayer compression and expansion) over the salt water subphase, which can result from their flexibility or large molecular areas in the monolayer (Figure S37); thus, no clear statements on the ion uptake can be made.

The expansion of the monolayers of type-I/II crown-ethers on addition of salts to the water subphase allows to suggest that monolayer is significantly destabilized due to electrostatic repulsion between metal ions. To confirm monolayer destabilization and establish ion selectivity by thiacalixcrowns, the change of the Gibbs energy for monolayer-expanding metal ions was calculated:

$$\Delta G = N_A \left(\int_0^{\pi_0} A_{\text{salt}} d\pi - \int_0^{\pi_0} A_{\text{water}} d\pi \right),$$

where π_0 is the upper limit of surface pressure and A_{salt} and A_{water} are the areas per molecule on the aqueous salt solution or pure water subphases, and N_A is the Avogadro's number [49]. The upper limit of surface pressure was taken to represent the monolayer before collapse and is specified in Table 6. In agreement with the largest monolayer expansion, the largest ΔG values were determined in the case of thiacalixcrowns **2a–c** and **5a–c** over the corresponding metal salt solutions.

Table 6. Excess Gibbs energy change ΔG ($\text{kJ} \times \text{mol}^{-1}$) calculated in the presence of $1 \times 10^{-2} \text{ M}$ metal salt solutions as subphase, with respect to pure water; $\pi_0 = 10$ (**2a**; **5a,b**), 15 (**2b**, **5c**), and 20 mN/m (**2c**).

Compound	ΔG (metal ion)		
2a	1.87 (Sr^{2+})	1.36 (Ba^{2+})	1.26 (Ag^+)
2b	6.52 (K^+)	2.83 (Rb^+)	2.46 (Gd^{3+})
2c	2.19 (K^+)	3.76 (Ag^+)	2.08 (Pb^{2+})
5a	1.95 (Na^+)	1.18 (Rb^+)	1.65 (Ca^{2+})
5b	1.27 (Na^+)	5.17 (Ca^{2+})	1.13 (Ba^{2+})
5c	1.02 (Rb^+)	1.94 (Cs^+)	1.32 (Ca^{2+})

Monolayer expansion of type-II receptors **5a–c** in the presence of $\text{Ca}(\text{NO}_3)_2$ in the water subphase could suggest sole responsibility of *1,3-alternate* topology for Ca^{2+} selectivity. To verify this hypothesis, a linear analog of thiacalixcrowns **5a–c**, compound **8** with two oxyethylene arms [17], was spread on the water subphase and its monolayer characteristics were measured (Figure 10). In analogy to the thiacalixcrowns, it was characterized by a take-off area of $217 \pm 7 \text{ \AA}^2$ and a liquid-expanded state of the monolayer ($C_s^{-1} = 37 \text{ mN/m}$), whereas near-zero SPOT could be caused by parallel arrangement of oxyethylene chains at the air–water interface. On addition of $\text{Ca}(\text{NO}_3)_2$ to the water subphase, the monolayer slightly expanded to $234 \pm 7 \text{ \AA}^2$ ($\Delta G = 1.08 \text{ kJ} \times \text{mol}^{-1}$ at $\pi_0 = 15 \text{ mN/m}$) and SPOT increased from 90 to 182 mV, whereas the UVRAS spectra did not change ($\lambda_{\text{max}} = 271 \text{ nm}$, Figure S38). These experiments demonstrate that the assembly of oxyethylene units into crown-4–6 macrocycle on *1,3-alternate* topology are crucial for effective Ca^{2+} uptake at the air–water interface.

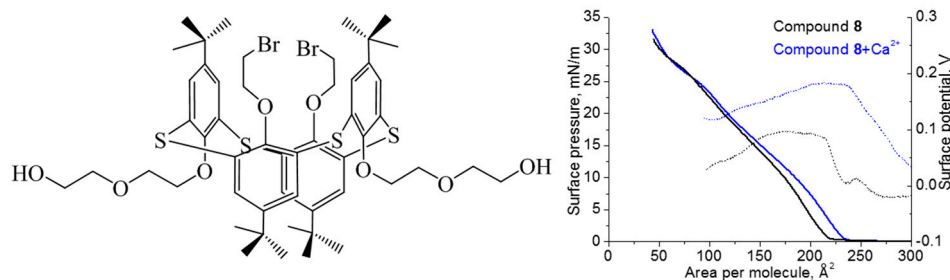


Figure 10. The surface pressure/SPOT–area isotherms of monolayers of compound **8** on water or $1 \times 10^{-2} \text{ M}$ $\text{Ca}(\text{NO}_3)_2$ subphase and the proposed orientation of compound **8** in the monolayer. $c = 1 \times 10^{-4} \text{ M}$ in CHCl_3 .

Previous experiments with crown-ether hemicyanine dyes confirmed that effective “oxygen crown-ether–metal ion” interactions occur only at initial stage of monolayer formation before CHCl_3 evaporation [50–52], and this interaction can alter the molecular arrangement in the monolayer. According to this model, the influence of cation on monolayer formation correlates with ion–receptor complementarity. To reveal the effect of residual CHCl_3 solvent on cation binding by crown-ether fragment in the ligands at the air–water interface, the ligand **5c** was spread over pure water subphase and, as CHCl_3 evaporation was complete, the aliquot of CsNO_3 was added to the water subphase under the monolayer. The maximum surface pressure for so-formed monolayer decreases as compared to one formed on CsNO_3 solution, indicating that the associates formed upon monolayer compression are destabilized (Figure 11). The kink at $\pi = 10 \text{ mN/m}$ also disappears; however, the take-off area remains the same, which allowed us to state that Cs^+ –thiacalixcrown interactions could occur without CHCl_3 and the change of take-off area is a reliable criterion of ion–ligand interactions for the thiacalixcrowns under study. On the contrary, crown-ether cavity is more accessible for solvent molecules in type-I receptors **2a–c** and the effect of residual CHCl_3 solvent on ion–monolayer interactions could be

remarkable. A comparison of the π - A isotherm of the monolayer of compound **2c** over the pure water subphase with those for the monolayers formed over the AgNO_3 aqua solution subphase and ones under which AgNO_3 was added after CHCl_3 evaporation confirmed the role of organic solvent in ion interactions and showed that the monolayer expansion is lower when the salt is added after the evaporation of CHCl_3 .

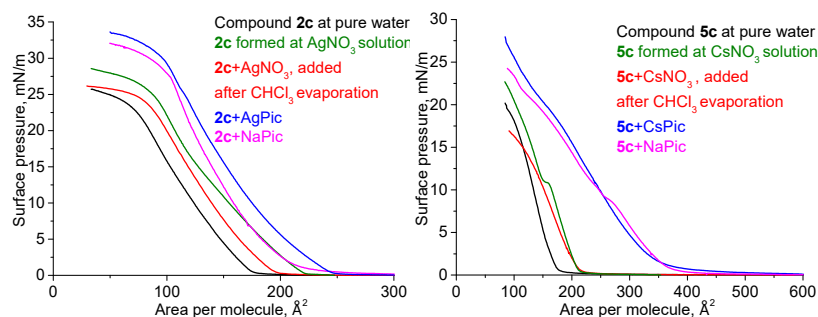


Figure 11. The surface pressure/SPOT-molecular area isotherms of monolayers of thiocalixcrowns **2c** and **5c** on water or 1×10^{-2} M aqueous salt solution subphase. The concentration in CHCl_3 is 1×10^{-4} M.

It could be suggested that picrate salts facilitate cation uptake by crown-ethers as compared to nitrate salts (by decreasing the energy of complexation and energy of phase transfer). A difference between the π - A isotherms of the monolayers of compound **2c** on AgPic and NaPic solutions (Figure 11) shows that Ag^+ vs. Na^+ selectivity is preserved in the case of picrate salts. Moreover, larger shifts of the take-off areas correlated with the larger destabilization of compound **2c** monolayer over picrate salt solution as compared to that over nitrate salt solution ($\Delta G = 6.56 \text{ kJ} \times \text{mol}^{-1}$ with AgPic vs. $\Delta G = 3.76 \text{ kJ} \times \text{mol}^{-1}$ with AgNO_3). In contrast, the π - A isotherms of the monolayer of type-II compound **5c** recorded over NaPic or CsPic solutions were identical except for the kink at $\pi \approx 10 \text{ mN/m}$ in case of NaPic . Such coincidence of the isotherms could be interpreted as a trend of hydrophobic Pic^- to form mixed monolayers with surfactants at the air-water interface through interactions between aromatic rings [53], which hampers analysis of cation binding from monolayer isotherm data.

Ion binding selectivity by thiocalixcrowns is summarized in Table 7 and again emphasizes the effect of topology of the ligands and environment. Gas-phase ion selectivity is governed by charge interactions and size fit of crown-ether unit with metal ions, which results in the most abundant peaks of alkali metal complexes of calixcrown-ethers, whereas liquid-phase extraction conditions favor Ag^+ binding due to solvated crown-ether cavity, and alkali metal ion selectivity could arise only when the crown-ether is hindered from solvent molecules (type-II receptors **5b,c**). The origin of a different ion selectivity of the crown-ether ligands at the air-water interface is considered in Section 2.6.

Table 7. Ion selectivity of thiocalixcrowns **2** and **5** in liquid and gas phases and air-water interface.

Conditions of Interaction	Ligand					
	2a	2b	2c	5a	5b	5c
Liquid-liquid interface ¹	Ag^+	Ag^+	Ag^+	Ag^+	Ag^+/Rb^+	Cs^+
Air-water interface ²	Sr^{2+}	K^+	Ag^+	Na^+	Ca^{2+}	Cs^+
Gas phase ³	Li^+	Na^+	K^+	Li^+/Na^+	K^+	Li^+/Cs^+

Evaluated from ¹ extractability, ² the Gibbs free energy of spreading films, and ³ peak abundance.

2.6. Mechanism of Metal Ion Binding by Thiocalixcrowns at Different Interfaces

The contribution of solvent seems to result in identical ion selectivity of the crown-ether ligands **2** and **5** at CH_2Cl_2 -water and air-water interfaces. However, a comparison of ion binding selectivity under these conditions (Table 7) reveals a number of differences.

Firstly, there is no change of the π -A isotherms of type-II thiacalixcrowns over AgNO_3 water subphase. To reveal a binding motif of Ag^+ ions and verify the role of S atoms in extraction of crown-ether ligands that was postulated in Section 2.2, complexation-induced shifts of NMR resonances of compound **6c** were analyzed (Table 8). On addition of 1 eq. AgClO_4 to compound **6c** in CDCl_3 (Figure S39), the signals of crown-ether are deshielded by 0.20–0.27 ppm, which indicates its coordination. Proximal Ph units could be involved in Ag^+ complexation through ion- π interactions or orbital interactions with S bridges, as evidenced by their downfield shift by 0.10 ppm. NMR spectra were recorded 1 h after preparation of solution and did not change within next 24 h, as well as upon the addition of larger amounts of AgClO_4 . Therefore, the absence of monolayer expansion of type-II thiacalixcrowns can be rationalized by steric hindrance of S atoms at air-water interface. Consequently, ion binding selectivity under these conditions is governed by the size fit of crown-ether cavity and metal ion in analogy to the gas-phase interactions (compound **5a**- Na^+ and compound **5c**- Cs^+ , Table 8). In contrast to 1,3-alternate stereoisomers, a positive cooperativity between S and O atoms can be achieved in *cone* thiacalixcrowns **2a**-**c** upon Ag^+ binding. There are downfield shifted signals of benzene rings (ca. 0.10 ppm) and upfield shifted signal of the ArOCH_2 unit in ^1H NMR spectrum of compound **2c** (Table 8, Figure S39), which is indicative of O_3S binding mode of Ag^+ . Blue-shifted π - π^* absorption bands at 282 and 303 nm, along with a hyperchromic effect in the former case in UV/visible spectra of compound **2c** with 1–10 eq. AgClO_4 (Figure 12), further support the involvement of OH groups and S atoms in Ag^+ binding. A decrease in the absorbance of crown-ether **2c** at 303 nm up to 4 equiv. of AgClO_4 suggests that one molecule of thiacalixcrown receptor binds several Ag^+ ions and is evidenced by the MALDI mass peaks corresponding to $[\text{M}-\text{H}+2\text{Ag}]^+$ and $[\text{M}-2\text{H}+3\text{Ag}]^+$ (Table S1). Notably, the signal of CH_2 -1 shifts upfield, which can be caused by the cleavage of H-bonds with OH group. Given a downfield shift of CH_2 -2,3, these results suggest exocyclic O_3S coordination of Ag^+ with phenolic O atom and two O atoms in crown-ether (Figure 12).

Table 8. CS differences ($\Delta\delta$, ppm) of compounds **6c**/**2c** upon the addition of AgClO_4 . Positive values indicate a downfield shift, negative values indicate an upfield shift. $\text{H}_{\text{Ar-1}}$ stands for the proton of ArOMe/ArOH unit, $\text{H}_{\text{Ar-2}}$ stands for the proton of Ar ring linked to crown-ether macrocycle.

Compound	$\text{H}_{\text{Ar-1}}$	$\text{H}_{\text{Ar-2}}$	CH_2 -1	CH_2 -2	CH_2 -3	CH_2 -4	CH_2 -5	OMe
6c	0.10	0.05	0.25	0.20	0.27	0.27	0.21	-0.08
2c	0.17	0.12	-0.41	0.08	0.16	-0.01	-0.02	n/a

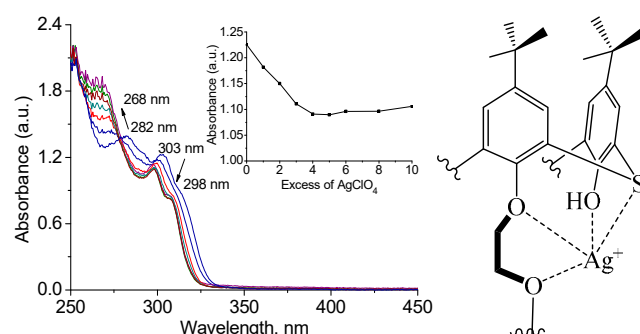


Figure 12. Evolution of UV/visible absorption spectra of compound **2c** ($c = 1 \times 10^{-4}$ M in CH_2Cl_2) on the addition of 1–10 eq. AgClO_4 and proposed binding mode of compound **2c** with Ag^+ ions in solution.

In spite of the ion selectivity of compound **2c** towards Ag^+ both at air-water and CH_2Cl_2 -water interfaces (Table 6), the involvement of S atoms in Ag^+ binding at the air-water interface could not be deduced, because they seem not to be immersed into the water subphase due to their hydrophobicity, and there is an air-water boundary between S

bridges and Ag^+ ions. To estimate the role of S atoms in compound **2c** in Ag^+ binding in Langmuir monolayers, monolayer characteristics of model compound **9** in *cone* topology, with bromopropyl fragments instead of crown-ether macrocycle, over pure water and AgNO_3 water subphases were compared (Figure S40). Nearly identical π -A isotherms of monolayers in both cases indicate that OH groups without crown-ether fragment cannot effectively bind Ag^+ ions at the air-water interface. Exocyclic coordination of Ag^+ with compound **2c** suggests that crown-ether cavity in type-I ligands could not accommodate metal ions effectively due to solvation. A synergism between crown-ether and OH moieties could, thus, be proposed to interpret binding selectivity at air-water interface towards metal ions, of which the radius is larger than crown-ether cavity (compound **2a**— Sr^{2+} and compound **2b**— K^+ , Table 6).

Ion selectivity of crown-ether conjugates in compounds **2a** and **5b** towards Sr^{2+} and Ca^{2+} (Table 6) is particularly interesting in spite of the evidence of alkali metal binding at the air-water interface. This difference poses two questions: (1) why there was no extraction selectivity towards Ca^{2+} by ligand **5b** and Sr^{2+} by ligand **2a**; (2) why should there be selectivity towards mentioned metal ions vs. alkali metal ions at the air-water interface. The first question can be addressed by recalling a contribution of ion transfer from water to CH_2Cl_2 into extraction, because multiple-charged Ca^{2+} and Sr^{2+} ions require higher energy for transfer than single-charged alkali-metal and Ag^+ ions. The second question was partially addressed in Section 2.5 regarding exocyclic coordination of alkaline-earth metal ions by type-I calixcrown **2a** and cation- π interactions of alkaline-earth metal ions with crown-ethers **5a,b** under lateral confinement. Due to the fact that the crown-ether unit is solvated in type-I receptors and the size fit of the crown-ether cavity and alkali metal ion is no longer decisive, a double-charged Sr^{2+} could stabilize exocyclic coordination mode in compound **2a** better than single-charged alkali metal ions. In analogy, solvation of crown-ether cavity in type-II receptors could decrease the contribution of the size fit in compound **5b**, making the cation- π interactions more important in ion selectivity, which are again stronger in the case of Ca^{2+} ions.

To estimate the possibility of **5b**-Ca complex formation and its influence on UV/visible spectra, quantum chemical computations were carried out. To simplify geometry optimizations and calculations of vertical shifts at DFT, the structures of model compound **5b'** with a shorter propyl chain on the lower rim and corresponding **5b'**-Ca complex were considered. Crown-ether macrocycle of the complex is predicted to be more symmetrical than that of ligand and the crown-ether-Ca fragment is bent to the aryl ring that is declined from the C_{2v} axis of the molecule. This is accompanied by the formation of short contacts between Ca and O/ipso-C atoms of the neighboring aryl ring (2.64 and 2.65 Å, respectively) (Figure 13). Similar conformational changes of crown-ether unit in 1,3-alternate calixcrowns upon complexation were evidenced in single crystals [54].

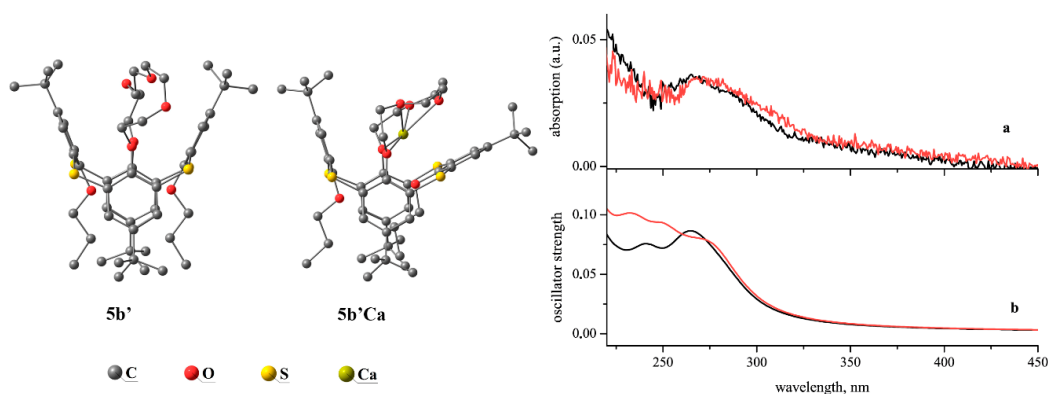


Figure 13. Optimized structures of model ligand **5b'** and complex **5b'**-Ca (left) and (right) (a) experimental UVRAS spectra of ligand **5b** over pure water subphase and over $\text{Ca}(\text{NO}_3)_2$ solution and (b) calculated UV spectra of ligand **5b'** and complex **5b'**-Ca (**5b**, **5b'**—black; **5b+Ca(NO₃)₂**, **5b'-Ca**—red).

Theoretical UV/visible spectrum of **5b'**-Ca complex shows a ca. 10 nm red shift of the low-energy absorption band compared to the one of **5b'** (Figure 13b), in good agreement with the experimental data (Figure 13a). The analysis of the frontier molecular orbitals shows that the corresponding band in the spectrum of the ligand is caused by the intraligand charge transfer, whereas in the case of **5b'**-Ca, this band contributes to the ligand-to-metal charge transfer (Figure S41).

3. Materials and Methods

Organic solvents were purified by known procedures [55]; the reagents were used as received. Water was deionized on an Adrona Crystal purification system up to the conductivity of 0.055 $\mu\text{S}/\text{cm}$. Known procedures were employed to synthesize *p*-tert-butylthiacalix[4]arene **1** [56], dialkylated thiacalixarenes **3** [26] and **4** [27], and thiacalix-crowns **2a-c** [24] and **6a-c** [13,25].

All NMR experiments were performed with Bruker AVANCE-400/500 MHz (400.05/500.13 MHz for ^1H NMR and 100.6/125.8 MHz for ^{13}C NMR) spectrometers equipped with a Bruker multinuclear z-gradient inverse probe head capable of producing gradients of 50 $\text{G}\cdot\text{cm}^{-1}$. The NMR spectra were recorded at $T = 295$ and 303 K. Chemical shifts are reported in the δ (ppm) scale relative to the ^1H (7.26 ppm) and ^{13}C (77.2 ppm) signals of CDCl_3 and coupling constants are denoted in Hz. The FT-PGSE experiments were performed by a bipolar pulse pair-stimulated echo-longitudinal eddy current delay (BPP-STE-LED) sequence [57] and repeated at least three times. All separated peaks were analyzed and the average values for the species were presented. The temperature was maintained at 303 K with a 640 L/h airflow rate to avoid heat fluctuations due to sample heating during the magnetic field pulse gradients. After Fourier transformation and baseline correction, the diffusion dimension was processed with the TopSpin3.2 program. Self-diffusion constants D_s were calculated by exponential fitting of the data from individual columns of the pseudo 2D matrix. Single components have been assumed for the fitting routine. Standard deviations of self-diffusion constants were less than 5%. Hydrodynamic radius R_h was calculated by the Einstein-Stokes equation:

$$R_h = \frac{k_B T}{6\pi\eta D_s},$$

where k_B is Boltzmann constant and η is dynamic viscosity of solvent (5.05×10^{-4} Pa s for CDCl_3).

MALDI mass spectra were recorded on an UltraFlex III TOF/TOF mass spectrometer (Bruker Daltonik GmbH, Bremen, Germany) in a linear mode using a Nd:YAG laser, $\lambda = 266$ nm. The sample solutions were applied to the MTP AnchorChipTM metallic target by the dried drop method. To evaluate gas-phase interactions with metal ions, an aliquot of 10 μL of a solution of thiacalix[4]arene-crown-ethers **2a-c** and **5a-c** (CHCl_3 , 1 mg/mL) was mixed with 10 μL of an aqueous solution of all metal nitrates under study at a concentration of 10 mg/mL. A total of 0.5 μL of the matrix solution and 0.5 μL of the sample were successively applied to the target and evaporated. *p*-Nitroaniline (10 mg/mL in CH_3CN) was used as the matrix. Positively charged ions were recorded. The data were obtained using the Flex Control program and processed using the FlexAnalysis 3.0 program.

IR spectra were recorded in KBr on a Bruker Vector 22 spectrometer at $\lambda = 400\text{--}4000$ cm^{-1} .

Synthesis of Compounds **5a-c**

Compound **3** (1 eq.), triphenylphosphine (6 eq.), and glycol (5 eq.) were suspended in 30 mL toluene and diethyl azodicarboxylate (6 eq.) was added dropwise at 0 $^\circ\text{C}$. The reaction mixture was stirred 8 h, at 20 $^\circ\text{C}$, and then for 8 h, at 40 $^\circ\text{C}$. The solvent was removed under reduced pressure and methanol (50 mL) was added to the residue; the precipitate was centrifuged, filtered, and purified by column chromatography (hexane:ethylacetate = 4:1).

Compound **5a**. Yield 1.22 g (75%). $T_m = 202$ $^\circ\text{C}$. R_f (*n*- C_6H_{14} :EtOAc = 6:1) 0.54. ^1H NMR (CDCl_3): 7.38 (s, 4H, H_{12}), 7.32 (s, 4H, H_3), 4.01 (m, 4H, H_7), 3.78 (t, 4H, J 8.4, H_{16}), 3.51

(m, 4H, H₈), 2.51 (s, 4H, H₉), 1.32 (s, 18H, H₆), 1.29 (s, 18H, H₁₅), 1.36–1.20 (m, 40H, H_{17–26}), 0.90 (t, 6H, J 6.8, H₂₇). ¹³C NMR (CDCl₃): 158.1 (C_{1i}), 156.4 (C_{10i}), 146.1 (C_{4i}), 145.9 (C_{13i}), 128.9 (C₃), 128.4 (C_{2i}), 128.1 (C_{11i}), 127.1 (C₁₂), 71.3 (C₇), 70.2 (C₁₆), 68.8 (C₈), 68.5 (C₉), 34.5 (C_{5i}), 34.4 (C_{14i}), 32.1 (C₁₇), 31.6 (C₁₅), 31.5 (C₆), 30.3 (C₁₈), 29.8 (C_{19–22}), 29.5 (C₂₃), 28.5 (C₂₄), 26.0 (C₂₅), 22.9 (C₂₆), 14.3 (C₂₇). *m/z* (MALDI) (%) 1194.2 (100) [M+Na]⁺. Anal. calcd. for C₇₀H₁₀₆O₆S₄: % C 71.75, H 9.12; found: C 71.62; H 9.15. IR (KBr, $\tilde{\nu}/\text{cm}^{-1}$) 2924 (C–H), 1436 (C_{Ar}–C_{Ar}), 1264 (C_{Ar}–O–C_{Alk}), 1086 (C_{Alk}–O–C_{Alk}). UV (CHCl₃, 10^{−5} M (ϵ , M^{−1} cm^{−1})) 268 nm (35126).

Compound **5b**. Yield 0.24 g (14%). *T_m* = 161 °C. *R_f* (*n*-C₆H₁₄:EtOAc = 6:1) 0.30. ¹H NMR (CDCl₃): 7.34 (s, 4H, H₁₃), 7.29 (s, 4H, H₃), 3.91 (m, 4H, H₇), 3.75 (t, 4H, J 8.2, H₁₇), 3.60 (m, 4H, H₈), 3.38 (m, 4H, H₉), 2.99 (m, 4H, H₈), 1.36 (s, 18H, H₆), 1.28 (s, 18H, H₁₆), 1.33–1.20 (m, 40H, H_{18–27}), 0.90 (t, 6H, J 6.0, H₂₈). ¹³C NMR (CDCl₃): 156.5 (C_{1i}), 156.4 (C_{11i}), 146.1 (C_{4i}), 145.9 (C_{14i}), 128.1 (C_{2i}), 127.8 (C_{12i}), 126.9 (C₃), 126.2 (C₁₃), 73.7 (C₇), 71.5 (C₁₇), 70.4 (C₈), 68.5 (C₉), 65.5 (C₁₀), 34.5 (C_{5i}), 34.4 (C_{15i}), 32.1 (C₁₈), 31.7 (C₁₆), 31.5 (C₆), 30.2 (C₁₉), 29.9 (C₂₀), 29.8 (C_{21–23}), 29.5 (C₂₄), 28.8 (C₂₅), 26.0 (C₂₆), 22.8 (C₂₇), 14.3 (C₂₈). *m/z* (MALDI) (%) 1237.7 (100) [M+Na]⁺. Anal. calcd. for C₇₂H₁₁₀O₇S₄: % C 71.12, H 9.12; found: C 71.25, H 9.10. IR (KBr, $\tilde{\nu}/\text{cm}^{-1}$) 2925 (C–H), 1442 (C_{Ar}–C_{Ar}), 1264 (C_{Ar}–O–C_{Alk}), 1089 (C_{Alk}–O–C_{Alk}). UV (CHCl₃, 10^{−5} M (ϵ , M^{−1} cm^{−1})) 267 nm (29669).

Compound **5c**. Yield 0.22 g (12%). *T_m* = 211 °C. *R_f* (*n*-C₆H₁₄:EtOAc = 6:1) 0.21. ¹H NMR (CDCl₃): 7.34 (s, 4H, H₁₄), 7.31 (s, 4H, H₃), 3.92 (m, 4H, H₇), 3.76 (t, 4H, J 8.2, H₁₈), 3.55 (s, 4H, H₁₁), 3.47 (m, 4H, H₉), 3.44 (m, 4H, H₁₀), 3.02 (m, 4H, H₈), 1.33 (s, 18H, H₆), 1.28 (s, 18H, H₁₇), 1.29–1.03 (m, 40H, H_{19–28}), 0.89 (t, 6H, J 6.8, H₂₉). ¹³C NMR (CDCl₃): 156.8 (C_{1i}), 156.7 (C_{12i}), 146.2 (C_{4i}), 145.9 (C_{15i}), 128.3 (C_{2i}), 127.8 (C_{13i}), 127.5 (C₃), 126.7 (C₁₄), 71.6 (C₇), 71.4 (C₁₈), 70.8 (C₈), 69.6 (C₉), 68.6 (C₁₀), 67.2 (C₁₁), 34.5 (C_{5i}), 34.4 (C_{16i}), 32.1 (C₁₉), 31.6 (C₁₇), 31.5 (C₆), 30.2 (C₂₀), 29.9 (C₂₁), 29.8 (C_{22–24}), 29.5 (C₂₅), 28.7 (C₂₆), 25.9 (C₂₇), 22.9 (C₂₈), 14.3 (C₂₉). *m/z* (MALDI) (%) 1300.2 (100) [M+Na]⁺. Anal. calcd. for C₇₄H₁₁₄O₈S₄: % C 70.54, H 9.12; found: C 70.78, H 9.14. IR (KBr, $\tilde{\nu}/\text{cm}^{-1}$) 2924 (C–H), 1444 (C_{Ar}–C_{Ar}), 1268 (C_{Ar}–O–C_{Alk}), 1091 (C_{Alk}–O–C_{Alk}). UV (CHCl₃, 10^{−5} M (ϵ , M^{−1} cm^{−1})) 268 nm (38642).

Extraction of metal picrates from water into CH₂Cl₂ followed a typical procedure and was conducted in triplicates to ensure reproducibility. Picric acid (HPic), alkali metal hydroxides, and metal (Ca, Ba, Mg, Sr, Ag, Pb, Eu, Tb, Gd) nitrates were dissolved in H₂O to the final concentration [HPic]₀ = 2 × 10^{−4} M and [MOH(MNO₃)]₀ = 10^{−2} M. Tris buffer was added to metal nitrates (except for AgNO₃) up to pH = 5.8 to avoid hydrolysis. Metal picrates were prepared by mixing aqueous solutions of HPic and metal hydroxides/nitrates in a 1:1 volume ratio. A total of 4 mL of ligands **2**, **5**, and **6** in CH₂Cl₂ (*c* = 4 × 10^{−4} M) was added to 4 mL of aqueous metal picrates. The biphasic system was stirred for 30 min at room temperature and, then, maintained for 15 min for phase separation. The UV/Vis absorption spectra of the aqueous phase were recorded using an AvaSpec-2048 fiber optic spectrophotometer (Avantes, Apeldoorn, the Netherlands) in the wavelength range of 200–500 nm with a resolution of 1 nm before and after extraction and maximum absorbances (*A*₀ and *A*_{*i*}, respectively) were recorded at $\lambda_{\text{max}} = 355$ nm. The extraction percentage (%E) was calculated as follows:

$$\%E = \frac{A_0 - A_i}{A_0} \times 100$$

DLS measurements were performed on a Zetasizer Nano particle size analyzer (Malvern Panalytical, Malvern, UK) in PCS1115 glass cuvettes thermostated at 25 °C. Three independent experiments were recorded for each sample; data were processed by Malvern DTS program.

The Langmuir method was used for monolayer formation by compounds **2**, **5**, and **6**. The UV/Vis absorption spectra of the CHCl₃ solutions of thiocalixcrowns **2**, **5**, and **6** were recorded on an AvaSpec-2048 spectrophotometer to control their concentration before spreading onto the water subphase; the spectrophotometer was equipped with a reflectometric probe at a distance of ca. 1 mm from the water subphase and perpendicular

to the water subphase to record UVRAS spectra of the monolayers using the method from [58]. Monolayers of the ligands **2**, **5**, and **6** were formed from CHCl_3 solutions (1×10^{-5} – 1×10^{-4} M) spread onto the water subphase with a microsyringe at the air–water interface on a KSV NIMA Teflon trough (Biolin Scientific, Gothenburg, Sweden) equipped with a Pt Wilhelmy plate and two polyacetal barriers. SPOT was monitored (with an accuracy of ± 2 mV) using KSV SPOT1 instrument (Biolin Scientific, Sweden) with a vibrating plate electrode at the distance of ca. 1 mm from the water subphase and a stainless steel counter electrode immersed in water. The surface dipole moment of molecules μ_{\perp} and compressibility modulus C_s^{-1} were calculated as follows:

$$\mu_{\perp} = \frac{A\Delta V}{12\pi}; C_s^{-1} = -A \left(\frac{\partial \pi}{\partial A} \right)_T,$$

where A is the molecular area, ΔV is surface potential at A , and π is surface pressure [45].

The following monolayer production conditions were employed: the time of spreading solvent evaporation was 15 min, monolayer compression rate was $5 \text{ cm}^2/\text{min}$, and $t = 25$ °C. The KSV Nima/Attension 2.2 and Origin programs were used for processing surface pressure/SPOT–molecular area data. Monolayers were vertically deposited onto quartz (Flyuorit, St.-Petersburg, Russia), which was degreased with EtOH and washed with water before use. A 10^{-2} M solution of metal salts in water subphase was used for complexation study.

AFM measurements were carried out on a MultiMode V scanning probe microscope (Veeco, United States) in tapping mode using RTESP rectangular cantilevers (Veeco) equipped with silicone probes. Resonance frequency of these cantilevers falls within the range of 250–350 kHz and the probe curvature radius is 10–13 nm. Microscopy images were recorded at the resolution of 512×512 points per frame at the scanning rate of 1 Hz; external distortions with a frequency down to 0.5 Hz were eliminated using an SG0508 anti-vibration system. Results of AFM scanning were processed and surface profiles were constructed using Nanoscope 7.0 program package. The mean surface roughness R_a at $1 \times 1 \mu\text{m}$ sections and topographic histogram are also given. 1D (for one line of scan section) roughness was calculated as follows:

$$R_a = -A \sum_{j=1}^N |r_j|, \text{ where } r_j = z_j - \bar{z}.$$

Full geometry optimizations of ligands **2**, **5**, and **6** were carried out using Priroda 16 quantum chemical program at DFT (Perdew–Burke–Ernzerhof (PBE) functional and basis set of triple- ζ quality (3z)) [59,60]. DFT calculations of solvation of the ligands including their further geometry optimization with Becke 3-parameter Lee–Yang–Parr (B3LYP) functional and 6-31G basis set with the assumption of solvent (polarizable continuum model (PCM)/solvation model based on density (SMD)) were run using Gaussian 09 suit of programs [61]. Computations of compounds **5b'** and **5b'**–Ca were performed using Gaussian 16 suit of programs [62] and def-TZVP (triple-zeta valence polarization) basis set [63]. Wood–Boring Stuttgart effective core potentials [64] were implied for Ca atom. The ground-state structures were optimized at DFT using the B3LYP functional [65,66]. The D3 London dispersion correction was applied as implemented in Gaussian [67]. The electronic spectra were simulated using time-dependent DFT [68–70] by calculating the first 50 vertical excitations from the ground state (S_0) equilibrium geometries with cam-B3LYP long-range-corrected functional, which yield good results for charge-transfer systems [71–73]. Vertical transitions were broadened with Gaussian function of full width at half maximum of 0.24 eV. The dipole length formalism was used to calculate the oscillator strengths. The excitation energies were consistently red-shifted by 0.4 eV upon cam-B3LYP calculations in order to better match experimental spectral curves.

Supplementary Materials: Supplementary Materials can be found at <https://www.mdpi.com/article/10.3390/ijms22073535/s1>.

Author Contributions: Conceptualization, A.M., S.K., S.S. (Sofiya Selektor), S.S. (Svetlana Solovieva), and I.A.; methodology, A.M.; validation, A.M., A.Y., and T.G.; formal analysis, T.G., R.N., and V.S.; investigation, A.M., A.Y., E.T., O.B., G.N., and V.S.; resources, O.B., S.K., and V.S.; data curation, A.M.; writing—original draft preparation, A.M., A.Y., T.G., R.N., E.T., O.B., G.N., and V.S.; writing—review and editing, A.M., S.K., S.S. (Sofiya Selektor), S.S. (Svetlana Solovieva), and I.A.; visualization, A.M.; supervision, A.M., S.S. (Svetlana Solovieva), and I.A.; project administration, A.M.; funding acquisition, A.M. All authors have read and agreed to the published version of the manuscript.

Funding: This research and APC were funded by the Russian Foundation for Basic Research (project no. 20-33-70204). The work was partially funded by the subsidy allocated to Kazan Federal University for the state assignment in the sphere of scientific activities 0671-2020-0063.

Institutional Review Board Statement: Not applicable.

Informed Consent Statement: Not applicable.

Data Availability Statement: Not applicable.

Acknowledgments: The authors are grateful to the Assigned Spectral-Analytical Center of Shared Facilities for Study of Structure, Composition and Properties of Substances and Materials of the Federal Research Center of Kazan Scientific Center of Russian Academy of Sciences (CSF-SAC FRC KSC RAS) for technical support.

Conflicts of Interest: The authors declare no conflict of interest.

Abbreviations

MALDI	Matrix-assisted laser desorption–ionization
CS	Chemical shift
NMR	Nuclear magnetic resonance
PC	Pinched cone
DC	Distorted cone
IR	Infrared
DLS	Dynamic light scattering
FT-PGSE	Fourier transform pulsed-gradient spin-echo
PSD	Particle size distribution
DFT	Density functional theory
TR	Transfer ratio
AFM	Atomic force microscopy
SPOT	Surface potential
UVRAS	UV/visible reflection–absorption spectroscopy
BPP-STE-LED	Bipolar pulse pair–stimulated echo-longitudinal eddy current delay
PBE	Perdew–Burke–Ernzerhof
B3LYP	Becke, 3-parameter, Lee–Yang–Parr
PCM	Polarizable continuum model
SMD	Solvation model based on density
TZVP	Triple-zeta valence polarization

References

1. Huskens, J.; Prins, L.J.; Haag, R.; Ravoo, B.J. *Multivalency: Concepts, Research & Applications*; Wiley: Chichester, UK, 2018. [\[CrossRef\]](#)
2. Yamada, S. Cation– π interactions in organic crystals. *Coord. Chem. Rev.* **2020**, *415*, 213301. [\[CrossRef\]](#)
3. Neri, P.; Sessler, J.L.; Wang, M.-X. *Calixarenes and Beyond*; Springer: New York, NY, USA, 2016. [\[CrossRef\]](#)
4. Schneider, H.-J. Strain effects determine the performance of artificial allosteric systems: Calixarenes as models. *Chem. Commun.* **2019**, *55*, 3433–3444. [\[CrossRef\]](#)
5. Atanassova, M.; Kurteva, V. Synergism as a phenomenon in solvent extraction of 4f-elements with calixarenes. *RSC Adv.* **2016**, *6*, 11303–11324. [\[CrossRef\]](#)

6. Kumar, R.; Sharma, A.; Singh, H.; Suating, P.; Kim, H.S.; Sunwoo, K.; Shim, I.; Gibb, B.C.; Kim, J.S. Revisiting fluorescent calixarenes: From molecular sensors to smart materials. *Chem. Rev.* **2019**, *119*, 9657–9721. [[CrossRef](#)] [[PubMed](#)]
7. Kim, H.J.; Lee, M.H.; Mutihac, L.; Vicens, J.; Kim, J.S. Host–guest sensing by calixarenes on the surfaces. *Chem. Soc. Rev.* **2012**, *41*, 1173–1190. [[CrossRef](#)]
8. Ovsyannikov, A.; Solovieva, S.; Antipin, I.; Ferlay, S. Coordination polymers based on calixarene derivatives: Structures and properties. *Coord. Chem. Rev.* **2017**, *352*, 151–186. [[CrossRef](#)]
9. Casnati, A.; Pochini, R.; Ungaro, R.; Bocchi, C.; Ugozzoli, F.; Egberink, R.J.M.; Struijk, H.; Lugtenger, R.; de Jong, F.; Reinhoudt, D.N. 1,3-Alternate calix[4]arene-crown-5 conformers: New synthetic ionophores with better K⁺/Na⁺ selectivity than valinomycin. *Chem. Eur. J.* **1996**, *2*, 436–445. [[CrossRef](#)]
10. Kumar, M.; Kumar, N.; Bhalla, V. Ratiometric detection of Hg²⁺ ions: An allosterically synchronized Hg²⁺/Li⁺ switch based on thiacalix[4]crown. *Dalton Trans.* **2011**, *40*, 5170–5175. [[CrossRef](#)]
11. Bouhroum, S.; Arnaud-Neu, F.; Asfari, Z.; Vicens, J. Ionic recognition by thiacalixarenes: Binding of alkali and heavy metal ions by thiacalix[4]arene-bis-crown[n]ethers. *Russ. Chem. Bull.* **2004**, *53*, 1544–1548. [[CrossRef](#)]
12. Lee, J.K.; Kim, S.K.; Bartsch, R.A.; Vicens, J.; Miyano, S.; Kim, J.S. Rapid metal ions shuttling through 1,3-alternate thiacalix[4]crown tubes. *J. Org. Chem.* **2003**, *68*, 6720–6725. [[CrossRef](#)]
13. Csokai, V.; Grün, A.; Parlagh, G.; Bitter, I. Synthesis and alkali cation extraction ability of 1,3-alt-thiacalix[4]mono(crown) ethers. *Tetrahedron Lett.* **2002**, *43*, 7627–7629. [[CrossRef](#)]
14. Ghidini, E.; Ugozzoli, F.; Ungaro, R.; Harkema, S.; El-Fadl, A.A.; Reinhoudt, D.N. Complexation of alkali metal cations by conformationally rigid, stereoisomeric calix[4]arene crown ethers: A quantitative evaluation of preorganization. *J. Am. Chem. Soc.* **1990**, *112*, 6979–6985. [[CrossRef](#)]
15. Park, J.-Y.; Kim, B.-C.; Park, S.-M. Molecular recognition of protonated polyamines at calix[4]crown-5 self-assembled monolayer modified electrodes by impedance measurements. *Anal. Chem.* **2007**, *79*, 1890–1896. [[CrossRef](#)]
16. Zhang, S.; Song, F.; Echegoyen, L. Synthesis, self-assembled monolayers and alkaline earth metal ion recognition of *p*-*tert*-butylcalix[4]arene derivatives. *Eur. J. Org. Chem.* **2004**, *2004*, 2936–2943. [[CrossRef](#)]
17. Muravev, A.A.; Solovieva, S.E.; Kochetkov, E.N.; Mel'nikova, N.B.; Safiullin, R.A.; Kadirov, M.K.; Latypov, S.K.; Antipin, I.S.; Konovalov, A.I. Thiacalix[4]monocrowns substituted by sulfur-containing anchoring groups: New ligands for gold surface modification. *Macroheterocycles* **2013**, *6*, 302–307. [[CrossRef](#)]
18. Jággerszki, G.; Grün, A.; Bitter, I.; Tóth, K.; Gyurcsányi, R.E. Ionophore–gold nanoparticle conjugates for Ag⁺-selective sensors with nanomolar detection limit. *Chem. Commun.* **2010**, *46*, 607–609. [[CrossRef](#)]
19. Ahn, J.; Lim, N.Y.; Park, J.S.; Choi, Y.; Jung, J.H. Fabrication of calix[4]arene-attached mesoporous ammonium molybdophosphate-silica hybrid and its application as an adsorbent for cesium ions. *New J. Chem.* **2017**, *41*, 3196–3203. [[CrossRef](#)]
20. Luo, L.; Zhang, X.; Feng, N.; Tian, D.; Deng, H.; Li, H. Cation-induced pesticide binding and release by a functionalized calix[4]arene molecular host. *Sci. Rep.* **2015**, *5*, 8982. [[CrossRef](#)] [[PubMed](#)]
21. Capuzzi, G.; Fratini, E.; Dei, L.; LoNostro, P.; Casnati, A.; Gilles, R.; Baglioni, P. Counterion complexation of calixarene ligands in monolayers and micellar solutions. *Colloid Surf. A* **2000**, *167*, 105–113. [[CrossRef](#)]
22. Nag, R.; Vashishtha, M.; Rao, C.P. Switching the ion selectivity from Fe³⁺ to Al³⁺ by a triazole-appended calix[4]arene-based amphiphile. *ChemistrySelect* **2018**, *3*, 1248–1256. [[CrossRef](#)]
23. Csokai, V.; Grün, A.; Bitter, I. Unprecedented cyclisations of calix[4]arenes with glycols under the Mitsunobu protocol. Part 1: A new perspective for the synthesis of calixcrowns. *Tetrahedron Lett.* **2003**, *44*, 4681–4684. [[CrossRef](#)]
24. van Leeuwen, F.W.B.; Beijleveld, H.; Kooijman, H.; Spek, A.L.; Verboom, W.; Reinhoudt, D.N. Synthesis and conformational evaluation of *p*-*tert*-butylthiacalix[4]arene-crowns. *J. Org. Chem.* **2004**, *69*, 3928–3936. [[CrossRef](#)]
25. Muravev, A.A.; Laishevstev, A.I.; Galieva, F.B.; Bazanova, O.B.; Rizvanov, I.K.; Korany, A.; Solovieva, S.E.; Antipin, I.S.; Konovalov, A.I. Azide-alkyne click approach to the preparation of dendrimer-type multi(thia)calix[4]arenes with triazole linkers. *Macroheterocycles* **2017**, *10*, 203–214. [[CrossRef](#)]
26. Latypov, S.K.; Kharlamov, S.V.; Muravev, A.A.; Balandina, A.A.; Solovieva, S.E.; Antipin, I.S.; Konovalov, A.I. Conformational diversity and dynamics of distally disubstituted calix and thiacalix[4]arenes in solution. *J. Phys. Org. Chem.* **2013**, *26*, 407–414. [[CrossRef](#)]
27. Muravev, A.A.; Yakupov, A.T.; Solovieva, S.E.; Antipin, I.S. A new approach to the synthesis of thiacycrowns on a thiacalix[4]arene scaffold. *Dokl. Chem.* **2019**, *487*, 188–191. [[CrossRef](#)]
28. Bitter, I.; Csokai, V. An expedient route to *p*-*tert*-butylthiacalix[4]arene 1,3-diethers via Mitsunobu reactions. *Tetrahedron Lett.* **2003**, *44*, 2261–2265. [[CrossRef](#)]
29. Muravev, A.A.; Solovieva, S.E.; Latypov, S.K.; Antipin, I.S.; Konovalov, A.I. Synthesis and characterization of thiacalix[4]monocrowns modified by thioether groups on the lower rim. *Phosphorus, Sulfur Silicon Relat. Elem.* **2013**, *188*, 499–502. [[CrossRef](#)]
30. Solovieva, S.E.; Muravev, A.A.; Zakirzyanov, R.T.; Latypov, S.K.; Antipin, I.S.; Konovalov, A.I. Synthesis, structure, and extraction ability of tetrasubstituted thiacalix[4]arenes with crown ether fragments on the lower rim. *Macroheterocycles* **2012**, *5*, 17–22. [[CrossRef](#)]

31. Lang, J.; Dvořáková, H.; Bartošová, I.; Lhoták, P.; Stibor, I.; Hrabal, R. Conformational flexibility of a novel tetraethylether of thiacalix[4]arene. A comparison with the “classical” methylene-bridged compounds. *Tetrahedron Lett.* **1999**, *40*, 373–376. [[CrossRef](#)]
32. Šimánová, M.; Dvořáková, H.; Stibor, I.; Pojarová, M.; Lhoták, P. Synthesis and conformational behaviour of lower-rim tetraacetylated thiacalix[4]arenes. *Tetrahedron Lett.* **2008**, *49*, 1026–1029. [[CrossRef](#)]
33. van Leeuwen, F.W.B.; Beijleveld, H.; Kooijman, H.; Spek, A.L.; Verboom, W.; Reinhoudt, D.N. Cation control on the synthesis of *p*-*t*-butylthiacalix[4](bis)crown ethers. *Tetrahedron Lett.* **2002**, *43*, 9675–9678. [[CrossRef](#)]
34. Danil de Namor, A.F.; Pugliese, A.; Casal, A.R.; Llerena, M.B.; Aymonino, P.J.; Sueros Velarde, F.J. The various factors involved in the extraction of alkali metal picrates by calixarene ester derivatives in the mutually saturated water–dichloromethane solvent system. *Phys. Chem. Chem. Phys.* **2000**, *2*, 4355–4360. [[CrossRef](#)]
35. Shannon, R.D. Revised effective ionic radii and systematic studies of interatomic distances in halides and chalcogenides. *Acta Cryst. A* **1976**, *32*, 751–767. [[CrossRef](#)]
36. Steed, J.W. First- and second-sphere coordination chemistry of alkali metal crown ether complexes. *Coord. Chem. Rev.* **2001**, *215*, 171–221. [[CrossRef](#)]
37. Chi, X.; Peters, G.M.; Hammel, F.; Brockman, C.; Sessler, J.L. Molecular recognition under interfacial conditions: calix[4]pyrrole-based cross-linkable micelles for ion pair extraction. *J. Am. Chem. Soc.* **2017**, *139*, 9124–9127. [[CrossRef](#)]
38. Ellis, R.J.; Meridiano, Y.; Muller, J.; Berthon, L.; Guilbaud, P.; Zorz, N.; Antonio, M.R.; Demars, T.; Zemb, T. Complexation-induced supramolecular assembly drives metal-ion extraction. *Chem. Eur. J.* **2014**, *20*, 12796–12807. [[CrossRef](#)]
39. Nayak, S.; Lovering, K.; Uysal, A. Ion-specific clustering of metal–amphiphile complexes in rare earth separations. *Nanoscale* **2020**, *12*, 20202–20210. [[CrossRef](#)]
40. Bourgeois, D.; El Maangar, A.; Dourdain, S. Importance of weak interactions in the formulation of organic phases for efficient liquid/liquid extraction of metals. *Curr. Opin. Colloid Interface Sci.* **2020**, *46*, 36–51. [[CrossRef](#)]
41. Smirnov, I.V.; Stepanova, E.S.; Tyupina, M.Y.; Ivenskaya, N.M.; Zaripov, S.R.; Kleshnina, S.R.; Solovieva, S.E.; Antipin, I.S. Americium and cesium extraction from alkaline media by calix[8]arenes with *p*-*tert*-butyl and isononyl substituents on the upper rim: Aggregation effect. *Macrocyclics* **2017**, *10*, 196–202. [[CrossRef](#)]
42. Muravev, A.A.; Trushina, E.A.; Yakupov, A.T.; Solovieva, S.E.; Antipin, I.S. Ag-selective nanotubes based on bithiacalix[4]arene with ethylene sulfide bridges. *Dokl. Chem.* **2019**, *487*, 212–214. [[CrossRef](#)]
43. Sieffert, N.; Chaumont, A.; Wippf, G. Importance of the liquid–liquid interface in assisted ion extraction: New molecular dynamics studies of cesium picrate extraction by a calix[4]arene. *J. Phys. Chem. C* **2009**, *113*, 10610–10622. [[CrossRef](#)]
44. Muravev, A.; Gerasimova, T.; Fayzullin, R.; Babaeva, O.; Rizvanov, I.; Khamatgalimov, A.; Kadirov, M.; Katsyuba, S.; Litvinov, I.; Latypov, S.; et al. Thermally stable nitrothiacalixarene chromophores: Conformational study and aggregation behavior. *Int. J. Mol. Sci.* **2020**, *21*, 6916. [[CrossRef](#)]
45. Gaines, G.L.J. *Insoluble Monolayers at Liquid–Gas Interfaces*; Wiley: New York, NY, USA, 1966.
46. Muravev, A.A.; Agarkov, A.S.; Galieva, F.B.; Yakupov, A.T.; Bazanova, O.B.; Rizvanov, I.K.; Shokurov, A.V.; Zaitseva, A.V.; Selektor, S.L.; Solovieva, S.E.; et al. New terpyridine derivatives of thiacalix[4]arenes in solution and at the water–air interface. *Russ. Chem. Bull.* **2020**, *69*, 339–350. [[CrossRef](#)]
47. Moradi, M.; Tulli, L.G.; Nowakowski, J.; Baljovic, M.; Jung, T.A.; Shahgaldian, P. Two-dimensional calix[4]arene-based metal-organic coordination networks of tunable crystallinity. *Angew. Chem. Int. Ed.* **2017**, *56*, 14395–14399. [[CrossRef](#)]
48. Dinadayalane, T.C.; Hassan, A.; Leszczynski, J. A theoretical study of cation– π interactions: Li^+ , Na^+ , K^+ , Be^{2+} , Mg^{2+} and Ca^{2+} complexation with mono- and bicyclic ring-fused benzene derivatives. *Theor. Chem. Acc.* **2012**, *131*, 1131. [[CrossRef](#)]
49. Lonetti, B.; Lo Nostro, P.; Ninham, B.W.; Baglioni, P. Anion effects on calixarene monolayers: A Hofmeister series study. *Langmuir* **2005**, *21*, 2242–2249. [[CrossRef](#)]
50. Selektor, S.L.; Shcherbina, M.A.; Bakirov, A.V.; Batat, P.; Grauby-Heywang, C.; Grigorian, S.; Arslanov, V.V.; Chvalun, S.N. Cation-controlled excimer packing in Langmuir–Blodgett films of hemicyanine amphiphilic chromoionophores. *Langmuir* **2016**, *32*, 637–643. [[CrossRef](#)]
51. Shokurov, A.V.; Shcherbina, M.A.; Bakirov, A.V.; Alexandrova, A.V.; Raitman, O.A.; Arslanov, V.V.; Chvalun, S.N.; Selektor, S.L. Rational design of hemicyanine Langmuir monolayers by cation-induced preorganization of their structure for sensory response enhancement. *Langmuir* **2018**, *34*, 7690–7697. [[CrossRef](#)] [[PubMed](#)]
52. Shokurov, A.V.; Alexandrova, A.V.; Lukovskaya, E.V.; Arslanov, V.V.; Selektor, S.L. The effect of alkyl substituent length on receptor properties of dithiaaza-crown-hemicyanine monolayers. *Macrocyclics* **2017**, *10*, 560–566. [[CrossRef](#)]
53. Leontidis, E. Chaotropic salts interacting with soft matter: Beyond the lyotropic series. *Curr. Opin. Colloid Interface Sci.* **2016**, *23*, 100–109. [[CrossRef](#)]
54. Thuéry, P.; Nierlich, M.; Lamare, V.; Dozol, J.-F.; Asfari, Z.; Vicens, J. Bis(crown ether) and azobenzocrown derivatives of calix[4]arene. a review of structural information from crystallographic and modelling studies. *J. Incl. Phenom. Macrocycl. Chem.* **2000**, *36*, 375–408. [[CrossRef](#)]
55. Armarego, W.L.F.; Armarego, W.L.F. *Purification of Laboratory Chemicals*; Butterworth-Heinemann: Oxford, UK, 2009.
56. Iki, N.; Kabuto, C.; Fukushima, T.; Kumagai, H.; Takeya, H.; Miyanari, S.; Miyashi, T.; Miyano, S. Synthesis of *p*-*tert*-butylthiacalix[4]arene and its inclusion property. *Tetrahedron* **2000**, *56*, 1437–1443. [[CrossRef](#)]

57. Wu, D.; Chen, A.; Johnson, C.S. An improved diffusion-ordered spectroscopy experiment incorporating bipolar-gradient pulses. *J. Magn. Reson., Ser. A* **1995**, *115*, 260–264. [[CrossRef](#)]
58. Stuchebryukov, S.D.; Selektor, S.L.; Silantieva, D.A.; Shokurov, A.V. Peculiarities of the reflection-absorption and transmission spectra of ultrathin films under normal incidence of light. *Prot. Met. Phys. Chem. Surf.* **2013**, *49*, 189–197. [[CrossRef](#)]
59. Perdew, J.P.; Burke, K.; Ernzerhof, M. Generalized gradient approximation made simple. *Phys. Rev. Lett.* **1996**, *77*, 3865–3868. [[CrossRef](#)]
60. Laikov, D.N. A new class of atomic basis functions for accurate electronic structure calculations of molecules. *Chem. Phys. Lett.* **2005**, *416*, 116–120. [[CrossRef](#)]
61. Frisch, M.J.; Trucks, G.W.; Schlegel, H.B.; Scuseria, G.E.; Robb, M.A.; Cheeseman, J.R.; Scalmani, G.; Barone, V.; Mennucci, B.; Petersson, G.A.; et al. *Gaussian 09*; Gaussian, Inc.: Wallingford CT, UK, 2009.
62. Frisch, M.J.; Trucks, G.W.; Schlegel, H.B.; Scuseria, G.E.; Robb, M.A.; Cheeseman, J.R.; Scalmani, G.; Barone, V.; Petersson, G.A.; Nakatsuji, H.; et al. *Gaussian 16, Revision B.01*; Gaussian, Inc.: Wallingford CT, UK, 2016.
63. Weigend, F.; Ahlrichs, R. Balanced basis sets of split valence, triple zeta valence and quadruple zeta valence quality for H to Rn: Design and assessment of accuracy. *Phys. Chem. Chem. Phys.* **2005**, *7*, 3297–3305. [[CrossRef](#)]
64. Bergner, A.; Dolg, M.; Küchle, W.; Stoll, H.; Preuß, H. Ab initio energy-adjusted pseudopotentials for elements of groups 13–17. *Mol. Phys.* **1993**, *80*, 1431–1441. [[CrossRef](#)]
65. Becke, A.D. Density-functional thermochemistry. III. The role of exact exchange. *J. Chem. Phys.* **1993**, *98*, 5648–5652. [[CrossRef](#)]
66. Lee, C.T.; Yang, W.T.; Parr, R.G. Development of the Colle-Salvetti correlation-energy formula into a functional of the electron-density. *Phys. Rev. B* **1988**, *37*, 785–789. [[CrossRef](#)] [[PubMed](#)]
67. Grimme, S.; Antony, J.; Ehrlich, S.; Krieg, H. A consistent and accurate ab initio parameterization of density functional dispersion correction (DFT-D) for the 94 elements H–Pu. *J. Chem. Phys.* **2010**, *132*, 154104. [[CrossRef](#)]
68. Bauernschmitt, R.; Ahlrichs, R. Treatment of electronic excitations within the adiabatic approximation of time dependent density functional theory. *Chem. Phys. Lett.* **1996**, *256*, 454–464. [[CrossRef](#)]
69. Bauernschmitt, R.; Häser, M.; Treutler, O.; Ahlrichs, R. Calculation of excitation energies within time-dependent density functional theory using auxiliary basis set expansions. *Chem. Phys. Lett.* **1997**, *264*, 573–578. [[CrossRef](#)]
70. Furche, F. On the density matrix based approach to time-dependent density functional response theory. *J. Chem. Phys.* **2001**, *114*, 5982–5992. [[CrossRef](#)]
71. Rudberg, E.; Salek, P. Calculations of two-photon charge-transfer excitations using Coulomb-attenuated density-functional theory. *J. Chem. Phys.* **2005**, *123*, 184108. [[CrossRef](#)] [[PubMed](#)]
72. Kobayashi, R.; Amos, R.D. The application of CAM-B3LYP to the charge-transfer band problem of the zincbacteriochlorin-bacteriochlorin complex. *Chem. Phys. Lett.* **2006**, *420*, 106–109. [[CrossRef](#)]
73. Cai, Z.L.; Crossley, M.J.; Reimers, J.R.; Kobayashi, R.; Amos, R.D. Density functional theory for charge transfer: The nature of the N-Bands of porphyrins and chlorophylls revealed through CAM-B3LYP, CASPT2, and SAC-CI calculations. *J. Phys. Chem. B* **2006**, *110*, 15624–15632. [[CrossRef](#)] [[PubMed](#)]